Vibrational Spectroscopy 144 (2026) 103913

Contents lists available at ScienceDirect

Vibrational Spectroscopy

journal homepage: www.elsevier.com/locate/vibspec

Probing the Effects of Plasma-Treated Water Solutions on Healthy and Head and Neck Cancer Cells via FTIR and Raman Spectroscopy

Maria Lasalvia [a], Vito Carlo Alberto Caponio [b], Roberto Gristina [c], Savino Cosmai [c], Vito Capozzi [a], Flavia Biamonte [d], Anna Martina Battaglia [d], Eloisa Sardella [c,**], Vittoria Perrotti [e,f,*], Giuseppe Perna [a]

[a] Department of Clinical and Experimental Medicine, Università degli Studi di Foggia, Via Napoli 20, Foggia I-71122 Italy
[b] Department of Life Sciences, Health and Health Professions, Link Campus University, Via del Casale Di San Pio V 44, Rome 00165, Italy
[c] Institute of Nanotechnology, CNR-NANOTEC c/o Department of Chemistry, Università di Bari Aldo Moro, via Orabona, 4, Bari 70126, Italy
[d] Department of Experimental and Clinical Medicine, "Magna Graecia" University of Catanzaro, Viale Europa, Catanzaro 88100, Italy
[e] Dept Innovat Technol Med & Dent, Università degli Studi "G. d'Annunzio" Chieti-Pescara, Chieti I-66100, Italy
[f] UdA-TechLab, Research Center, "G. d'Annunzio" University of Chieti-Pescara, Chieti, Italy

ARTICLE INFO

Keywords:
Cold atmospheric plasma
FTIR spectroscopy
Head and neck cancer
Plasma medicine
Plasma treated water solutions
Raman spectroscopy

ABSTRACT

Building on evidence that plasma-treated water solutions (PTWS) exhibit antitumor activity, this study investigated their selective effects on healthy keratinocytes versus head and neck cancer (HNC) cells. PTWS were generated from clinically approved rehydrating solutions supplemented with tyrosine (SIII-Tyr) and treated with oxygen or air plasma at different treatment times. Human keratinocytes (HaCaT) and HNC (FaDu and SAS) cells were exposed to different PTWS formulations for 30 min followed by 24-hours incubation in culture medium. Cells were analysed using Fourier Transform Infrared (FTIR) and Raman spectroscopy, with principal components analysis (PCA) to identify biochemical changes related to cytotoxicity. Results were correlated with cell viability (MTT assay) and intracellular reactive oxygen species (ROS) levels (flow cytometry). HaCaT cells showed minimal sensitivity, while FaDu and SAS cells were significantly affected. Notably, SAS cells exhibited over 90% mortality after exposure to PTWS oxy 20' sample. ROS levels increased in all cell lines following exposure to PTWS, but for HaCaT cells remained below the baseline ROS of untreated HNC. The highest ROS accumulation was observed in SAS cells treated with PTWS oxy 20', aligning with cytotoxicity data. PCA of FTIR and Raman spectra revealed distinct biochemical signatures in HNC cells, particularly under PTWS oxy 20' treatment exposure. Even under milder conditions (air 10'), significant spectral deviations between HNC and HaCaT cells suggested a potential window for selective action. These findings support PTWS selectivity against HNC cells. From a vibrational spectroscopy perspective, this study provides a novel, rapid, label-free tool combining FTIR with Raman to assess selective biochemical responses in HNC models. These results support future preclinical and translational applications.

1. Introduction

Head and neck cancer (HNC) comprises a heterogeneous group of malignancies arising from the mucosal surfaces of the oral cavity, pharynx, and larynx, and represents the sixth most common cancer worldwide [1]. Despite advances in diagnosis and treatment, the prognosis for patients with HNC remains suboptimal, particularly in locally advanced or recurrent/metastatic stages [2]. Standard therapeutic strategies - comprising surgery, radiotherapy, and chemotherapy - are often used in combination and guided by tumor stage, location, and patient-related factors, as recommended by current international guidelines (e.g., NCCN [3], ESMO [4]). Platinum-based chemotherapy, typically combined with radiation, is a cornerstone of treatment for advanced HNC. While this approach can improve locoregional control

* Correspondence to: Department of Innovative Technologies in Medicine & Dentistry, University "G. d'Annunzio", Chieti-Pescara, Via dei vestini 31, Chieti 66100, Italy.
** Correspondence to: CNR, Istituto di Nanotecnologia (CNR-NANOTEC), UoS Bari, c/o Dipartimento di Chimica, Università degli Studi di Bari Aldo Moro, via Orabona, 4, Bari 70126, Italy.
E-mail addresses: eloisa.sardella@cnr.it (E. Sardella), vittoria.perrotti@unich.it (V. Perrotti).

https://doi.org/10.1016/j.vibspec.2026.103913
Received 12 January 2026; Received in revised form 31 March 2026; Accepted 8 April 2026
Available online 9 April 2026

and survival, it is frequently associated with significant toxicity, including mucositis, xerostomia, dysphagia, immunosuppression, and long-term functional impairments that drastically impact patients' quality of life [5]. Moreover, the five-year relative survival was 61%, 49%, 41% and 25% for laryngeal, oral cavity, oropharyngeal and hypopharyngeal squamous cell carcinoma (SCC) [6], respectively with even lower rates for patients with HPV-negative tumors or recurrent/-metastatic disease. High recurrence rates and resistance to therapy further complicate disease management, highlighting an urgent need for innovative, more selective, and less toxic treatment modalities. In this challenging scenario, the intrinsic heterogeneity of HNC - both at the molecular and cellular levels - provides a strong rationale for exploring multimodal therapeutic approaches capable of targeting different tumor subpopulations.

Among emerging technologies, Cold Atmospheric Plasma (CAP) has gained increasing attention due to its potential as a selective anticancer agent [7,8]. Indirect application of CAP, through plasma-treated water solutions (PTWS), is emerging as promising anticancer tools due to its ability to deliver reactive oxygen and nitrogen species (RONS) in a controlled and selective manner and to induce oxidative stress and apoptosis preferentially in cancer cells while sparing healthy tissues, as reported in preclinical studies [9–11]. Although not necessarily curative, plasma-based therapies could play a valuable role as adjuvant treatments - contributing to tumor debulking, enhancing the efficacy of standard therapies, and potentially reducing the need for aggressive surgical interventions. Their selective mechanism of action against cancer cells also holds promise in minimizing side effects commonly associated with conventional treatments. As reported in literature PTWS can be effectively used to: promote sterilization and disinfection due to their efficacy against bacteria fungi [12] and viruses [13]; enhance regeneration of tissues and wound healing (WH) due to the inactivation of pathogens, activation of WH-relevant cytokines/growth factors and recruitment of immune cells into the wound area [14]; act as an anticancer tool toward many types of cancer cells due their ability to promote the formation of secondary singlet oxygen ($^1O_2$) and a synergistic effect of hydrogen peroxide (H_2O_2) with nitric oxides (NOx) [15,16] as well as the recruitment of immune cells in the tumor site [17,18]. The reactive species responsible of the most part of observed biological effects are quite stable oxygen species (O, O_3, $^1O_2$, H_2O_2, $O_2\bullet^-$/•OOH) and nitrogen species (•NO, $ONOO^-$ and $OONOO^-$, NO_2^-, NO_3^-). The concentration of H_2O_2 correlates with impaired cell viability and growth, positioning it as a potential biomarker for evaluating the efficacy of PTWS. However, compared to mock solutions following H_2O_2 dose-response curves, PTWS exhibits enhanced cytotoxicity, suggesting that additional plasma-generated reactive species contribute to its overall biological effect [19]. In our recently published study [9], we developed clinically relevant PTWS using SIII, a rehydrating electrolyte solution routinely used in clinical settings, as the liquid base. These solutions were enriched with tyrosine, a biomolecule that acts as a booster for RONS generation when exposed to volume and planar Dielectric Barrier Discharges (DBD) fed with air or pure O_2 [9].

Although efforts are being made, additional research is needed to clarify the specific molecular pathways and key regulatory points that dictate which of these processes are triggered in response to redox imbalance induced by CAP treatment. Unlike pharmaceutical agents, the effects of PTWS on cells depend on chemical composition of the liquid, time of cell exposure to PTWS as well as the type of the exposed cells [20]. When cells are exposed to the reactive oxygen and nitrogen species (RONS) present in PTWS, they undergo oxidative stress [21]. Lipids - particularly those with unsaturated fatty acid chains and polar regions containing nucleophilic heteroatoms - are major components of the cell membrane and primary targets of oxidation [22]. Lipid peroxidation can alter key membrane properties such as stability and permeability, potentially contributing to mechanisms of cell death, especially in cancer cells. Correlating cell exposure to exogenous RONS with measurable membrane oxidation is difficult, as, for example, oxidized lipid species may be highly reactive and short-lived or rapidly processed by cellular repair systems [23]. As a result, the extent to which PTWS-induced oxidative stress affects cell integrity, and whether this underlies selective cytotoxicity in cancer cells, remains almost unclear [7]. Recent advances in biomedical research have emphasized the intricate interdependence of cellular processes, which originate from molecular mechanisms and are critically governed by the structural and dynamic properties of biomolecules. Pathological conditions and pharmacological interventions can markedly affect the molecular architecture, composition, and dynamics of tissues, cells, and membranes [24]. Accordingly, a comprehensive understanding of structure-function relationships is fundamental for elucidating disease pathophysiology and the mechanisms underlying therapeutic efficacy.

Based on these considerations, and to achieve a more reliably selective PTWS treatment, it may be valuable to incorporate analytical techniques capable of distinguishing healthy from cancerous cells by leveraging their underlying biochemical differences. Since the transformation of healthy cells into cancerous ones involves molecular alterations in cellular components, biochemistry-based approaches could offer meaningful insights. These methods would not replace standard analyses but rather enhance them, contributing to a more mechanism-informed interpretation of treatment effects and to the rational optimization of PTWS generation and exposure parameters. Among these techniques, vibrational spectroscopy, specifically Fourier Transform Infrared (FTIR) absorption and Raman spectroscopy, has proven effective in probing the structural and dynamic features of biomolecules across a wide range of biological samples, including cells, tissues, fluids, and biopolymers [25–28].

In particular, FTIR and Raman spectroscopy enable the analysis of infrared radiation absorbed and inelastically scattered, respectively, by specific functional groups within cellular macromolecules, such as nucleic acids, proteins, and lipids, thereby generating a molecular fingerprint of the biological sample. FTIR microspectroscopy has been effectively applied to discriminate between malignant and healthy colon tissues by detecting characteristic differences in their absorption spectra [29,30]. Raman spectroscopy has also proven to be an effective technique for distinguishing between non-cancerous and cancerous human tissues and for characterizing the biochemical composition of tissue samples [31].

FTIR and Raman spectroscopies have proven effective in detecting biochemical changes in biological samples associated with disease onsets as well as chemical [32,33] or physical [34] treatments. Both techniques are non-invasive and non-destructive, require minimal sample preparation, and allow repeated measurements. FTIR analysis of cells is fast and yields spectra with high signal-to-noise ratio, however, it cannot be performed in water environments due to strong water absorption peaks (as O-H stretching at about 3300 cm^{-1} and O-H scissoring at about 1640 cm^{-1}) that significantly overlap with key spectral features of the sample. Consequently, the sample must be dried before measurements. Furthermore, FTIR transmission requires substrates transparent to IR radiation, excluding commonly used materials such as glass in certain spectral ranges. Instead, Raman spectroscopy enables analysis in an aqueous environment and on cells adhered to glass coverslips as the glass contribution is limited and can be excluded from the spectra. Raman also provides micrometric spatial resolution, allowing investigation of sub-cellular regions, whereas FTIR typically probes large areas collecting the contribution of multiple cells. The main limitation of Raman spectroscopy is the intrinsically low signal-to-noise ratio, due to the low probability of Raman scattering (approximately one photon in 10^8) [35]. Overall, the combined use of FTIR and Raman spectroscopies offers complementary biochemical information about the investigated samples.

This study introduces a novel application of combined FTIR and Raman analysis to monitor PTWS-induced biochemical alterations and to discriminate selective responses between healthy and cancer cells in HNC models, which has not been previously reported.

2. Materials and Methods

2.1. Plasma processing

The plasma treatment system, developed by E.S. and S.C. at CNR-NANOTEC, consists of a planar volume DBD device housed within a glass chamber (150 mm diameter), capable of treating up to 1 L of liquid per cycle. For the purposes of this study, 60 mL of liquid were used per experiment. This volume was selected based on preliminary tests that identified it as optimal for maintaining a balance between liquid volume and the concentration of reactive species generated under static conditions.

An Electrolyte Rehydrating III (SIII) (Fresenius Kabi, VR, Italy) solution supplemented with L-Tyrosine (Sigma aldrich, 300 mg/l) was treated indirectly, positioned 2 mm below the plasma discharge region. The discharge area corresponded to the size of the high-voltage (HV) copper electrode (76 mm in diameter, 0.5 mm thick), and the plasma effluents reached the liquid surface after passing through a grounded mesh placed 2 mm above it. The HV electrode, coated with a 1 mm-thick Pyrex dielectric, was powered by a microsecond-pulsed generator (Alma-Pulse; AlmaPlasma s.r.l.), operating at frequencies between 3 and 9 kHz, voltages ranging from 6 to 10 kV, and with duty cycles of 10% or 25% (i.e., 10 or 25 ms plasma on-time within a 100 ms 100 ms period).

Before each treatment, the gap between the discharge zone and the liquid was purged for 2 min with the selected gas feed. Plasma discharges were conducted at a constant gas flow rate of 1 $L{\cdot}min^{-1}$, and treatment durations ranged from 5 to 20 min. Given the recent rise in the cost of noble gases such as helium and argon, this study employed either pure oxygen (99.999%) or synthetic air (99.999%) as the feed gas for the DBD system.

2.2. Detection of RONS in PTWS

Hydrogen peroxide (H_2O_2) and nitrite ions (NO_2^-) were detected through UV–Vis spectrometry in the spectral range of 200–800 nm (5 nm resolution) by a Cary 60 UV-Vis spectrophotometer (Agilent, Santa Clara, CA). Disposable plastic cuvettes (Bio-Rad, Hercules, CA) with a semi-micro volume of 1 mL and 10 mm optical length were used. The samples were analysed within 30 min from the end of plasma processing. For all measurements, the blank sample was prepared using double distilled water instead of the sample, according to the manufacturer's protocols.

The H_2O_2 was quantified using a copper-phenanthroline assay developed in-lab [9]. The reaction was performed in 0.01 M sodium phosphate buffer (pH 7.00), prepared from Na_2HPO_4 (cat. no. 30427, Riedel-de Haën) and $NaH_2PO_4{\cdot}H_2O$ (Carlo Erba). Two reagents were used: 0.012 M $CuSO_4{\cdot}5H_2O$ (Sigma-Aldrich) in water and 0.06 M neocuproine (Sigma-Aldrich) in methanol. To 700 μL of sample (untreated or plasma-treated), 100 μL of each reagent was added in sequence: $CuSO_4$, buffer, then neocuproine. The reaction proceeded for 10 min, and the resulting colour remained stable for 20 min. Standard H_2O_2 solutions (0–300 μM) were prepared in SIII from a 30% w/w stock (cat. no. 95321; Sigma-Aldrich) for calibration. Baseline correction of spectra was performed using Origin Pro9. For PTWS samples, the untreated spectrum (H_2O_2-free) was subtracted after baseline correction, due to a shared absorbance peak at 454 nm.

The concentration of NO_2^- ions was determined using the Griess assay (Spectroquant® 1.14776.001, Merck) [36]. The reagent, in powder form, was added (13 mg) to 1 mL of sample in a cuvette. Sample pH was adjusted to 2–10. After vigorous mixing to dissolve the powder, the reaction proceeded for 10 min. The developed color was stable for 60 min. Calibration was done using standard $NaNO_2$ solutions (cat. no. S2252, ≥99.0%; Sigma-Aldrich) in SIII. The absorbance peak was centred at 525 nm.

2.3. Cell culture

HaCaT cell line, used as a model of healthy keratinocytes, was purchased from CliniSciences (#T0020001, Guidonia Montecelio, Roma, Italy) and cultured in DMEM/F12 (Gibco, Waltham, MA, USA) supplemented with heat-inactivated 5% FBS, 10 mM HEPES. The hypopharyngeal carcinoma cell line (FaDu) was obtained from American Type Culture Collection (ATCC #HTB-41, Rockville, MD, USA) and grown in Minimum Essential Medium (MEM) (Corning, Manassas, VA, USA) supplemented with 1% Non-Essential Amino Acids (Gibco, Waltham, MA, USA). The tongue carcinoma cell line (SAS) was kindly provided by Prof. Lorenzo Lo Muzio (University of Foggia, Italy). SAS was cultured in RPMI (Corning, Manassas, VA, USA). All media were supplemented with 10% heat-inactivated foetal bovine serum (FBS), 100 units/mL penicillin, and 100 μg/mL streptomycin (all from EuroClone S.p.A., Pero (Mi), Italy). The investigated cells were cultured for up to 1 month and maintained at 37 °C supplied with 5% CO_2 before PTWS exposure.

2.4. Cell Viability Assay

Cell viability was assessed using the 3-[4,5-dimethylthiazol-2-yl]-2,5-diphenyltetrazolium bromide (MTT) assay (Sigma-Aldrich, St. Louis, MO, USA) [37]. Briefly, 1×10^4 cells/well were seeded in 96-well flat-bottom plate. After 24 h of culture, the cells were washed three times with PBS and then covered with 1 mL of the different PTWS formulations. In parallel, a set of cells was incubated with the SIII-Tyr solution used as reference. At this stage, no culture medium was present, and the cells were exposed exclusively to the PTWS-air and PTWS-oxy obtained after 10 or 20 min of plasma treatment (hereafter referred to as 10′ and 20′, respectively). The cells were incubated with the PTWS for 30 min, after which the solutions were removed, the cells were washed twice with PBS, and the wells were refilled with fresh culture medium. Fresh MTT solution (5 mg/mL in PBS) was added to each well to achieve a final concentration of 0.5 mg/mL. After 4 h incubation, the medium was removed, and formazan crystals were solubilized in 200 μL of isopropanol (Sigma-Aldrich). Absorbance was measured at 595 nm using a Multiskan™ FC Microplate Photometer (Thermo Fisher Scientific, Waltham, United States) and expressed as a percentage of viability relative to SIII-Tyr cells at 24 h. All experiments were performed in triplicate.

2.5. Quantification of intracellular ROS

Intracellular ROS levels were quantified using the redox-sensitive probe 2′,7′-dichlorodihydrofluorescein diacetate (H2DCFDA; Thermo Fisher Scientific, Waltham, MA, USA) [38]. At a defined incubation time starting from the point in which the PTWS was replaced with cell culture medium, the last one was removed, and the cells were washed three times with PBS. Then cells were incubated with the probe for 10 min at 37 °C, according to the manufacturer's instructions. Fluorescence was analyzed by flow cytometry on a BD LSRFortessa™ X-20 (BD Biosciences, San Jose, CA, USA), with at least 2×10^4 cells acquired per condition. Data was processed using FlowJo™ software (Tree Star Inc., Ashland, OR, USA). Each experiment was performed in triplicate.

2.6. Sample preparation for spectroscopy measurements

CaF_2 disks (Crystran Ltd., Dorset, UK) were coated with poly-L-lysine to promote cell adhesion and then they were placed on the bottom of 6-well Petri dishes. Next, 2.5 mL of cell suspension (containing about 5×10^3 cells) was evenly distributed on each CaF_2 disk. Then, the disks with cells were exposed for 30 min to various PTWS, as well as some of them were incubated with the SIII-Tyr solution used as reference. Upon completion of the exposure period, the PTWS and SIII-Tyr solutions were replaced with complete culture medium. The cells were then incubated for 24 h at 37°C in a humidified atmosphere containing 5% CO_2. Post-

incubation, fixation of cells was performed using 3.7% paraformaldehyde in Phosphate Buffer Solution (PBS). After fixation, the cells were rinsed several times, first with PBS and then with distilled water (to remove PBS residues from the cell surface). Prior to FTIR spectroscopy analysis, the samples were stored in a desiccator.

Cells designated for Raman spectroscopy analysis were cultured on glass coverslips pre-coated with poly-L-lysine. Following exposure to the PTWS and incubation with SIII-Tyr solution for 30 min, the samples were incubated for 24 h at 37 °C in a 5% CO_2 humidified atmosphere. Subsequently, the cells were fixed with 3.7% paraformaldehyde in PBS solution. Prior to Raman spectral acquisition, the fixed cell samples were stored in PBS and rinsed with deionized water to remove residual salts.

2.7. Vibrational spectroscopy measurements

FTIR spectra were measured by means of a Vertex 70 interferometer (Bruker Optik GmbH) connected to HYPERION 2000 microscope (Bruker Optik GmbH). The spectra were measured in the transmission mode, with a mercury cadmium telluride (MCT) detector, cooled by liquid nitrogen, and using a 15 × objective. Each spectrum was recorded in the 900–3700 cm^{-1} spectral range with a resolution of 4 cm^{-1} and 64 scans. The sampling area was about 80 × 80 μm size, including 3–4 cells of each type. The background signal was collected in a spatial region free of cells but including the poly-L-lysine thin coating. For each experiment, about 40 sampling areas were measured. Data acquisition was done by means of Opus 8.7.41 software (Bruker Optik).

Raman spectra were measured with a Raman confocal microspectrometer (Labram from Jobin-Yvon Horiba, Montpellier, France), using an Olympus 100x oil-immersion objective, in the range 600–1800 cm^{-1}. Each Raman measurement was carried out by placing the glass coverslip containing the cells onto a home-made microscope slide provided with a well (whose size is equal to that of the coverslip), which was filled with PBS solution. The side of the coverslip where the cells adhered was placed in the PBS so that the laser beam through the glass coverslip probed fixed single cells kept in the PBS solution. Before measuring each Raman spectrum, an optical image of the single cell to be measured was obtained using a charge-coupled device (CCD) camera, in order to select the cell compartment from which to collect the signal. The 514.5 nm line of an Ar ion laser was focused on a cell volume including the nucleus, with a spot size having less than 1 μm diameter and a laser power of about 6 mW. The spectrum obtained from each single cell consisted of the average signal of three consecutive acquisitions of 10 s each. About 35 randomly chosen cells were measured for each of the three cell types and each of the different exposure conditions. The backscattered Raman light was analyzed by a diffraction grating with 600 grooves/mm and it was detected by a CCD. The spectral resolution was about 5 cm^{-1}/pixel. The background signal was measured within volumes where no cell was located.

2.8. Vibrational spectroscopy analysis

For each FTIR measurement the spectral ranges 900–1800 cm^{-1} and 2800–3700 cm^{-1} were separately analyzed. A baseline signal was subtracted from each spectrum, using a rubber band correction with 64 baseline points. Then, the obtained spectra were vector normalised and offset corrected (in order to shift the minimum absorption to zero value). These pre-processing procedures were performed independently for the two ranges of each FTIR spectrum by means of the Opus 8.7.41 software.

Each Raman spectrum was pre-processed by subtracting the measured background signal and the cell fluorescence and stray light signal. This latter was estimated according to the adaptive algorithm of the Spectragryph software (version 1.2.16.2023) [39], with a coarseness value of 40: such algorithm creates a baseline that fits to the lower part of the spectra to remove the underlying broad and featureless signals while keeping actual peaks. The background spectrum is due to the Raman signal of the glass coverslip and PBS solution, and it is mainly characterized by a strong band centred at about 940 cm^{-1}, related to the glass coverslip [40]; this band cannot be fully removed by means of the background subtraction. Therefore, because the presence of this spurious and cell-to-cell variable signal could affect the data analysis, only the 980–1800 cm^{-1} range of each spectrum was retained for further processing and analysis. Then, area normalization was performed in order to normalize each spectrum to the total amount of biological material in the sampling volume.

Second-derivative spectra, calculated using the Orange Data Mining software (version 3.38.1) [41], were used to determine the peak positions of the FTIR and Raman main features of the average spectra. Exploratory data analysis of FTIR and Raman spectra was performed by Principal Component Analysis (PCA) with Orange Data Mining software, in order to visualize the discrimination of the different types of samples (in the score plots) and the spectral variables to which this separation is related (in the loading plots). The comparison between the means of the distributions of PC score values was performed by means of the rank sum test using SigmaPlot software (version 15.1.1.26, Grafiti LLC, Palo Alto, California).

2.9. Statistical Analysis

Statistical analysis was performed using Prism 9 (version 9.01, GraphPad Software, San Diego, CA, USA). Two-way ANOVA by Dunnett's multiple comparisons test (ctrl *vs* PTWS treatment for each cell type separately) was applied for cell viability, while ordinary-one-way ANOVA with Dunnett's correction was used for intracellular ROS measurements. Data are expressed as mean ± standard deviation. Statistical significance was indicated on the plots as follows: $*p \leq 0.05$, $**p \leq 0.01$, $***p \leq 0.001$, $****p \leq 0.0001$, ns, not significant.

3. Results and discussion

To determine the most appropriate experimental conditions for eliciting a cellular response and based on the assumption that H_2O_2 concentration serves as a potential biomarker for assessing the efficacy of PTWS, we quantified H_2O_2 levels in PTWS generated under various experimental conditions. Alterations in duty cycle (Fig. 1a), applied frequency (Fig. 1b), and peak-to-peak voltage (Fig. 1c) within the tested parameter ranges did not yield statistically significant differences in H_2O_2 concentration (Fig. 1). In contrast, H_2O_2 levels exhibited a linear increase as a function of plasma treatment duration (Fig. 1d), indicating that, under the examined conditions, treatment time is the primary factor influencing H_2O_2 generation in the window of experimental conditions investigated.

The absence of significant changes in H_2O_2 concentration when modifying duty cycle, frequency, or peak-to-peak voltage within the selected parameter ranges, could be because these electrical parameters do not substantially alter the electron energy distribution, chemistry of the plasma phase and in turn the efficiency of plasma treatment. On the other hand, the duration of the treatment directly influences the total energy delivered to the plasma phase (energy dose) improving the production of RONS in the plasma phase. Moreover, long treatment times proportionally increases the number of plasma-liquid interaction events, thereby enabling more H_2O_2 precursors like OH radicals to dissolve and accumulate in the aqueous phase. As a result, treatment time becomes the dominant factor determining the final H_2O_2 concentration, while variations in the other parameters within the tested ranges are insufficient to promote the formation of different formulations of plasma treated liquids.

To enhance the prospects for future clinical application, we selected four PTWS formulations to be used two weeks after preparation. Based on the considerations outlined above, four experimental conditions were selected for subsequent analyses. All experiments were conducted at a peak-to-peak voltage of 10 kV, a frequency of 9 kHz, and in pulsed mode with a duty cycle of 25%. The experimental conditions were defined by

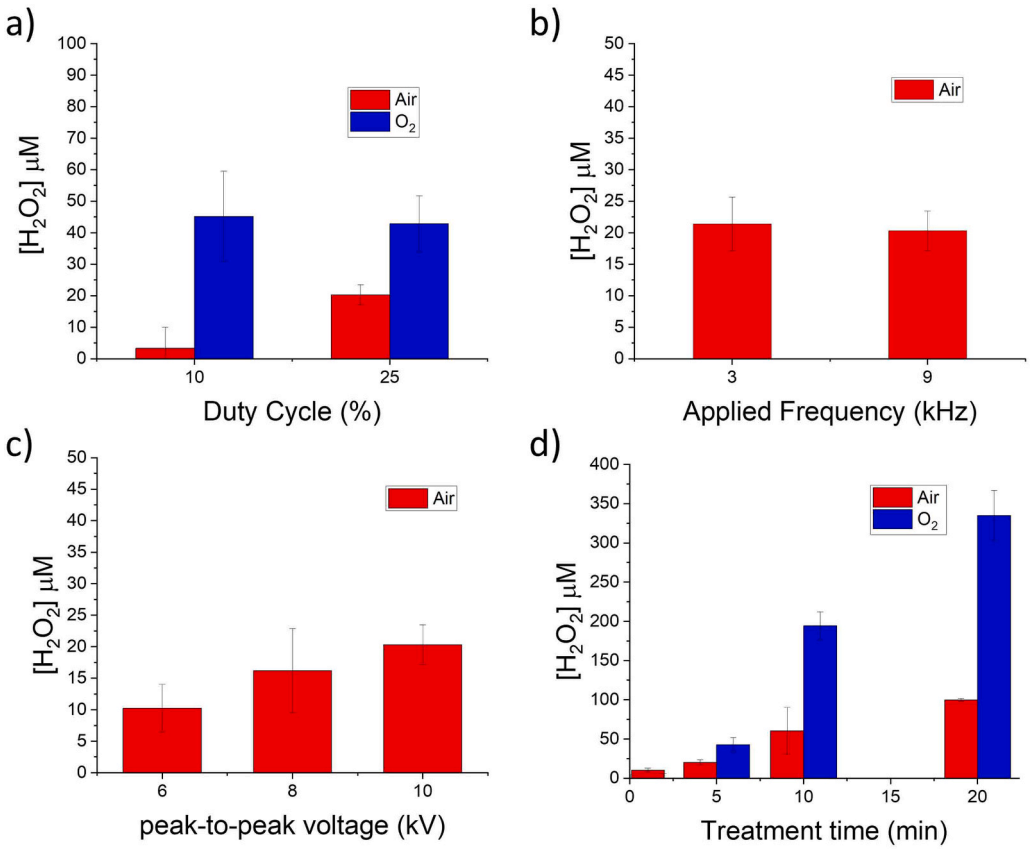

Fig. 1. H_2O_2 concentrations in PTWS generated under varying experimental conditions: (a) duty cycle (10% and 25%), (b) applied frequency (3 kHz and 9 kHz), (c) peak-to-peak voltage (6–10 kV), and (d) treatment time (1 min to 20 min). Data obtained using air (red) and O_2 (blue) as feed gases are shown. When one parameter is varied, the others are held constant at the following values: 100 ms period, 25% duty cycle, 9 kHz frequency, 10 kV peak-to-peak Voltage, 10 min treatment time, 1 SLM as gas flow rate.

varying the treatment duration (10 or 20 min) and the feed gas (i.e., air or oxygen). The samples are hereafter designated as: air 10′ (air as feed gas, 10 min treatment), air 20′ (air as feed gas, 20 min treatment), oxy 10′ (oxygen as feed gas, 10 min treatment), and oxy 20′ (oxygen as feed gas, 20 min treatment). The H_2O_2 and NO_2^- concentrations along with the corresponding experimental conditions in PTWS generated using either air or oxygen as the feed gas, across different treatment durations of PTWS after 15 days of storage at room temperature (RT) is reported in Table 1. Both H_2O_2 and NO_2^- concentrations, both in case of oxygen- and air-fed discharges, exhibit a linear correlation with treatment time still present after 15 days of storage at RT. In the samples prepared using oxygen as the feed gas, the nitrite concentration was below the detection limit.

The results in terms of quantification of H_2O_2 and NO_2^- both of aged samples and as prepared ones (with values in parentheses referring to fresh samples) are reported in Table 1 and compared. An increase in H_2O_2 concentration was observed after storage in PTWS, regardless of the feed gas used during plasma treatment. This behavior may be attributed to the involvement of tyrosine in the formation of secondary H_2O_2 [9]. In contrast, NO_2^- concentrations remained unchanged or showed a slight decrease. The observed decrease in nitrite levels during storage at room temperature likely reflects ongoing post-treatment chemistry in plasma-treated liquids, where reactive nitrogen and oxygen species continue to react, shifting the balance toward more stable nitrate (NO_3^-) formation or other oxidized nitrogen products, as reported in plasma treated water studies [42]. The mechanisms underlying these effects are beyond the scope of the present study and warrant further investigation.

MTT assay showed that none of the PTWS formulations, either generated in air or oxygen, induced a significant reduction in viability of healthy HaCaT keratinocytes (Fig. 2a). In contrast, FaDu cells showed a statistically significant reduction in viability, particularly after exposure to PTWS air or oxy 20' with decreases of approximately 20% and 35%, respectively. This effect was even more pronounced in SAS cells, which were the most sensitive among the cell lines tested. In these cells, viability decreased by ~20% upon exposure to PTWS air 20' by ~30% with PTWS oxy 10', and over 90% with PTWS oxy 20' (Fig. 2a).

To evaluate oxidative stress levels induced by the treatment, intracellular reactive oxygen species (ROS) were quantified using the non-specific redox-sensitive probe H₂DCFDA, analysed by flow cytometry (Fig. 2b). The analysis was conducted on cells exposed to all PTWS formulations, except for PTWS oxy 20', which was excluded due to its pronounced cytotoxicity resulting in insufficient viable material for analysis. Notably, after treatment with PTWS oxy 20', SAS cells exhibited > 90% cell death, leaving an insufficient number of viable cells to reach the minimum threshold (20,000 events) required to reliably perform ROS quantification by H₂DCFDA flow cytometry (Fig. 2b). As expected, untreated HaCaT cells exhibited the lowest basal ROS levels (mean fluorescence intensity [MFI]: 4453). In contrast, untreated FaDu and SAS cancer cells displayed much higher basal ROS levels (Fig. 2b, ctrl), on average 10-fold higher, with FaDu showing an MFI of 43562 and SAS reaching 52151. Upon PTWS treatment, HaCaT cells showed an approximate 4-fold increase in ROS levels, with a more substantial effect observed following exposure to 20 min treatment formulations, and a stronger ROS induction from PTWS oxy compared to PTWS air. However, even under the most cytotoxic condition (PTWS oxy 20'), ROS levels in HaCaT cells did not exceed the basal ROS levels of the other untreated cancer cells. In FaDu cells, ROS increase following PTWS

Table 1
Concentrations of H_2O_2 and NO_2 obtained in PTWS prepared at different experimental conditions and stored at RT for 15 days. Values of the concentrations measured at time zero, within the first 30 min following plasma treatment, are reported in parentheses, below the value measured after aging.

Name	Experimental plasma conditions	$[H_2O_2]$ μM	$[NO_2^-]$ μM
air 10'	Gas feed: 1SLM of Synthetic air Frequency: 9 kHz Applied Voltage: 10KV, Duty Cycle: 25% Pulsing Period: 100 ms Liquid: SIII-Tyr (Tyr 300 mg/L) Liquid volume: 60 mL plasma/liquid distance: 3 mm Treatment time: 10 min	163 ± 16 (145 ± 27)	42 ± 24 (69 ± 3)
air 20'	Gas feed: 1SLM of Synthetic air Frequency: 9 kHz Applied Voltage: 10KV, Duty Cycle: 25% Pulsing Period: 100 ms Liquid: SIII-Tyr (Tyr 300 mg/L) Liquid volume: 60 mL plasma/liquid distance: 3 mm Treatment time: 20 min	223 ± 40 (208 ± 60)	73 ± 31 (105 ± 3)
oxy 10'	Gas feed: 1SLM of O_2 Frequency: 9 kHz Applied Voltage: 10KV, Duty Cycle: 25% Pulsing Period: 100 ms Liquid: SIII-Tyr (Tyr 300 mg/L) Liquid volume: 60 mL plasma/liquid distance: 3 mm Treatment time: 10 min	251 ± 12 (194 ± 18)	3 ± 2 (0.7 ± 0.3)
oxy 20'	Gas feed: 1SLM of O_2 Frequency: 9 kHz Applied Voltage: 10KV, Duty Cycle: 25% Pulsing Period: 100 ms Liquid: SIII-Tyr (Tyr 300 mg/L) Liquid volume: 60 mL plasma/liquid distance: 3 mm Treatment time: 20 min	396 ± 125 (335 ± 32)	3 ± 2 (0.6 ± 0.4)

treatment was modest but statistically significant (MFI: from 61257 to 65630). In contrast, SAS cells showed a marked ROS increase, particularly with PTWS oxy 10', reaching an MFI of 107210.

To investigate whether the differences observed in the response of HNC cells compared to healthy cells correspond to underlying biochemical alterations, FTIR and Raman analyses were performed on cells exposed to PTWS and compared to those treated with the untreated liquid (SIII-Tyr).

The mean FTIR absorption and Raman spectra of the HaCaT, FaDu and SAS cells after exposure to PTWS oxy 10' and 20' and compared to those ones exposed to SIII-Tyr are shown in Fig. 3. Fig. 3a-c show the FTIR spectra in the 2800–3700 cm^{-1} range, while Fig. 3d-f present the spectra recorded between 900 and 1800 cm^{-1}. The corresponding Raman spectra are displayed in Fig. 3g-i. The labels in the left-hand plots refer to the spectral positions of the main absorption peaks and Raman features, whose attributions are reported in Table 2 in agreement with previously published results [43,44]. The spectral positions of such features were located according to the minima of second derivative signal, as shown in Figure S1. The features in the Raman spectra of FaDu and SAS cells whose spectral positions are slightly different from those of the corresponding spectra of HaCaT cells are labelled in Figs. 3h and 3i. The spectra of the HaCaT, FaDu and SAS cells after exposure to PTWS air, as well as those incubated with SIII-Tyr, are reported in Fig. 4. All the spectra in Figs. 3 and 4 have been vertically shifted for clarity.

It is important to note that FTIR spectra represent absorption signals averaged over groups of multiple individual cells, whereas Raman spectra are acquired from sub-nuclear regions within single cells. Consequently, the 2800–3700 cm^{-1} region of the FTIR spectra reflects contributions from lipid and protein components distributed throughout the entire cell volume, while the 900–1800 cm^{-1} region provides information on protein and nucleic acid components from the same cellular domain. In contrast, Raman spectra, collected from sub-nuclear regions, offer more localized insights, making them particularly useful for investigating potential effects of PTWS on nuclear constituents. Given the higher spatial resolution of Raman spectroscopy, several Raman peaks associated exclusively with nucleic acids, specifically at ~1380, ~1420, and ~1580–1585 cm^{-1}, along with the shoulder near ~1495 cm^{-1}, can be useful to determine whether exposure to PTWS elicits biochemical modifications in these critical nuclear components.

The major spectral peaks in the cells shown in Figs. 3 and 4 are nearly identical in both position and intensity, suggesting that the exposure does not cause major alterations in cellular architecture or the relative abundance of biochemical constituents across the three cell types. As anticipated, Raman spectra exhibit lower signal/noise ratios than FTIR spectra, reflecting the fact that FTIR is based on absorption of the energy of the incident photons, whereas Raman is based on rare inelastic scattering of the incident photons [35,45]. Consequently, variation in the FTIR dataset primarily reflects actual biochemical changes induced by cell exposure to PTWS and highlighting inter-cellular signal variability. In the case of Raman measurements, by contrast, spectral variability is further compounded by the lower signal-to-noise as well as intra-cellular biochemical heterogeneity.

To investigate the effects of exposure on the main cellular components, we selected the spectral features at 2850 and 2923 cm^{-1} in the FTIR spectra as representative of lipid components, the features at 1544 and 1654 cm^{-1} in FTIR spectra as representative of protein component and the signals at 970 and 1085 cm^{-1} in the FTIR spectra and at 1380, 1420, 1495, and 1580–1585 cm^{-1} in the Raman spectra as representative of nucleic acid components. Such investigated selected features are bold marked in Table 2. As for FTIR spectra, the peaks at 2850 and 2923 cm^{-1} were selected because they are the most intense peaks related to lipid components, just as the peaks at 1544 and 1654 cm^{-1} are the most intense peaks due to protein components, whereas the peaks at 970 and 1085 cm-1 are the only resolved peaks due to nucleic acids components. As for the peaks selected in the Raman spectra, they are those that, as shown in Table 2, are due exclusively to nucleic acid components, without overlap with other cellular components.

To probe the distinct effects of the tested PTWS on different cell types and to identify if the above selected spectral features related to lipids, proteins and nucleic acids are modified by exposure, we performed PCA of the FTIR and Raman spectral data. In particular, we investigated the score plots related to the PCs that best discriminate the spectra of cells subjected to different treatments, so that the corresponding loading plots provide information about eventual modification of the above selected spectral features and, consequently, of the corresponding functional groups within the cellular components.

The PCA score plot of the FTIR spectra in the 2800–3700 cm^{-1} region (Fig. 5a) reveals clear separation: spectra from HaCaT cells incubated with SIII-Tyr cluster distinctly from those of cells treated with oxy 10' or oxy 20' PTWS. Specifically, the PC1 scores for SIII-Tyr samples are negative, whereas spectra from PTWS-exposed cells predominantly occupy positive PC1 values (though a few spectra from exposed cells overlap with the negative range of the SIII-Tyr cluster). The distributions of PC1 score values are summarized by the box plots, whose parameters (median and 25th and 75th percentile values) are reported in Table 3, together with information about statistically significant differences between the three distributions. In particular, the data in Table 3 highlight that the differences between the distribution of PC1 score values of the SIII-Tyr incubated cells spectra and those of both the PTWS exposed cells spectra are statistically significant. The loading 1 plot in Fig. 5b points

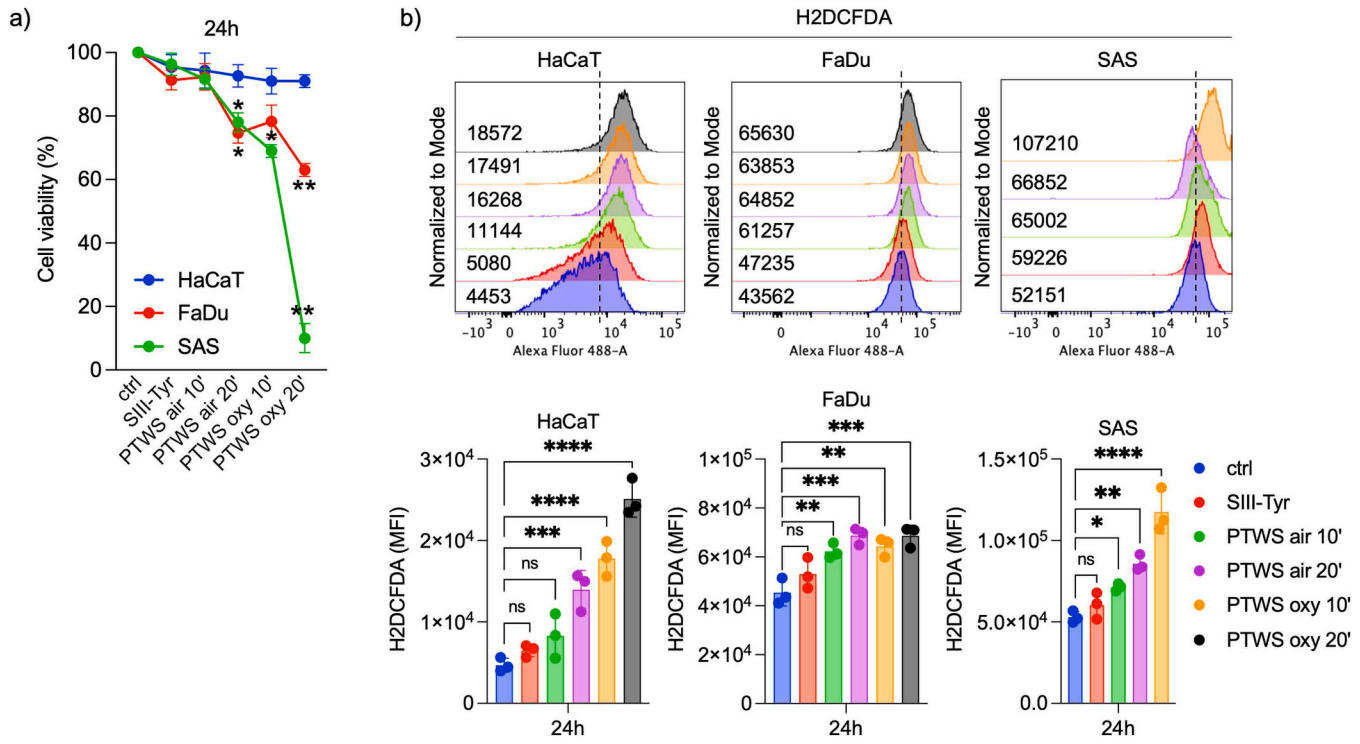

Fig. 2. A) Cell viability assessed by MTT assay in HaCaT, FaDu, and SAS cells following 30 minexposure to PTWS formulations (air 10′, air 20′, oxy 10′, oxy 20′) and subsequent culture for 24 h. B) Intracellular ROS levels measured by flow cytometry using the H2DCFDA probe under the same experimental conditions. Representative flow cytometry plots and histograms are shown. Data are representative of three independent biological replicates. Statistical significance: *p ≤ 0.05; **p ≤ 0.01; ***p ≤ 0.001; ****p ≤ 0.0001; ns, not significant.

out that the CH_2 stretching peaks of the methylene lipids bonds at 2850 and 2923 cm^{-1} are strongly involved in such a discrimination based on the PC1 score values. In fact, the positive values of some spectral peaks in a loading plot indicate that samples with positive scores have a larger relative content of the chemical components corresponding to those peaks. Therefore, Fig. 5b suggests that the relative content of the methylene lipids bonds is larger in PTWS exposed cells than in the SIII-Tyr incubated ones. The large negative band at about 3500 cm^{-1} corresponds to OH stretching vibrational mode and it might be due to difference of residual water content between the cells incubated with PTWS and those incubated with SIII-Tyr solution.

The increase of relative intensity of CH_2 methylene FTIR peaks has been previously reported for different human cells undergoing oxidative stress [46,47] and apoptosis [48,49]. This behaviour has been related to a higher acyl chain unsaturation level, which is known to happen with lipid peroxidation [50] and to the relative increase in phospholipids due to the formation of apoptotic bodies [48]. These results are consistent with the increase of intracellular ROS simulated by PTWS reported in Fig. 2B and with previous findings published by our group [51]: specifically, we detected apoptosis in several HNC cell lines upon treatment with PTWS.

The score plot in Fig. 5c, related to FTIR spectra of HaCaT cells in the 900–1800 cm^{-1} range, confirms a clear separation between the PC1 score values of cells incubated with SIII-Tyr and those exposed to PTWS, as also illustrated by the corresponding box plots. The distributions of PC1 scores for the SIII-Tyr group differ significantly from those of both PTWS-treated groups, while no statistically significant difference is observed between oxy 10' and oxy 20' samples (Table 3). The loading plot of PC1 in Fig. 5d shows that the absorption bands at 1654 and 1544 cm^{-1} exhibit decreased intensity following PTWS exposure, suggesting protein degradation or conformational changes. Similar decreases in protein-associated FTIR signals have been reported in the literature following exposure to pro-apoptotic agents such as usnic acid, which is also known to induce lipid peroxidation, depletion of glutathione resulting from the failure of redox machinery of cells after treatment [48]. Moreover, those studies also report an increased intensity ratio between a spectral band at ~1250 cm^{-1} (to which contributions arise from C-O-P stretching modes in phosphorylated lipids and proteins) and the amide I peak, attributed to oxidative stress induced by the acidic agent. This trend is consistent with our data by the slightly negative feature near 1250 cm^{-1} in the loading 1 plot of Fig. 5d. In contrast, no discernible changes were observed in spectral features attributable to the selected nucleic acid moieties (centered at 970 and 1085 cm^{-1}) in our spectra.

The score plot in Fig. 5e indicates that PC3 captures differences between Raman spectra of HaCaT cells incubated with SIII-Tyr and those exposed to PTWS. In contrast, the score values of PC1 and PC2 do not effectively distinguish among different experimental conditions, suggesting that the primary sources of spectral variance are unrelated to PTWS exposure, likely arising from other intrinsic or experimental factors, as previously discussed. In Fig. 5e, the PC3 score associated with the SIII-Tyr group are predominantly negative, whereas the majority of spectra from PTWS oxy exposed cells exhibit positive PC3 score values. Furthermore, the distribution of PC3 score values for the cells exposed to the two PTWS are largely overlapping, with no statistically significant difference between them, as shown by the corresponding box plots and reported in Table 3. Regarding the involvement of the selected nucleic acid-related functional groups in the cellular response to PTWS, the PC3 loading plot of Fig. 5f reveals only a slight intensity decrease at 1580 cm^{-1} following PTWS exposure. This minor spectral change suggests that PTWS induces minimal biochemical alterations in nuclear components of HaCaT cells, which is consistent with the findings obtained from FTIR analysis. The positive peak at centred at 1440 cm^{-1} and the negative peaks at about 1002 cm^{-1} and 1640–1680 cm^{-1} in Fig. 5f also confirm that lipid and protein components are mainly responsible for discriminating exposed and unexposed cells.

The PCA score plot of the FTIR spectra acquired in the 2800–3700 cm^{-1} region for cells exposed to PTWS air is shown in

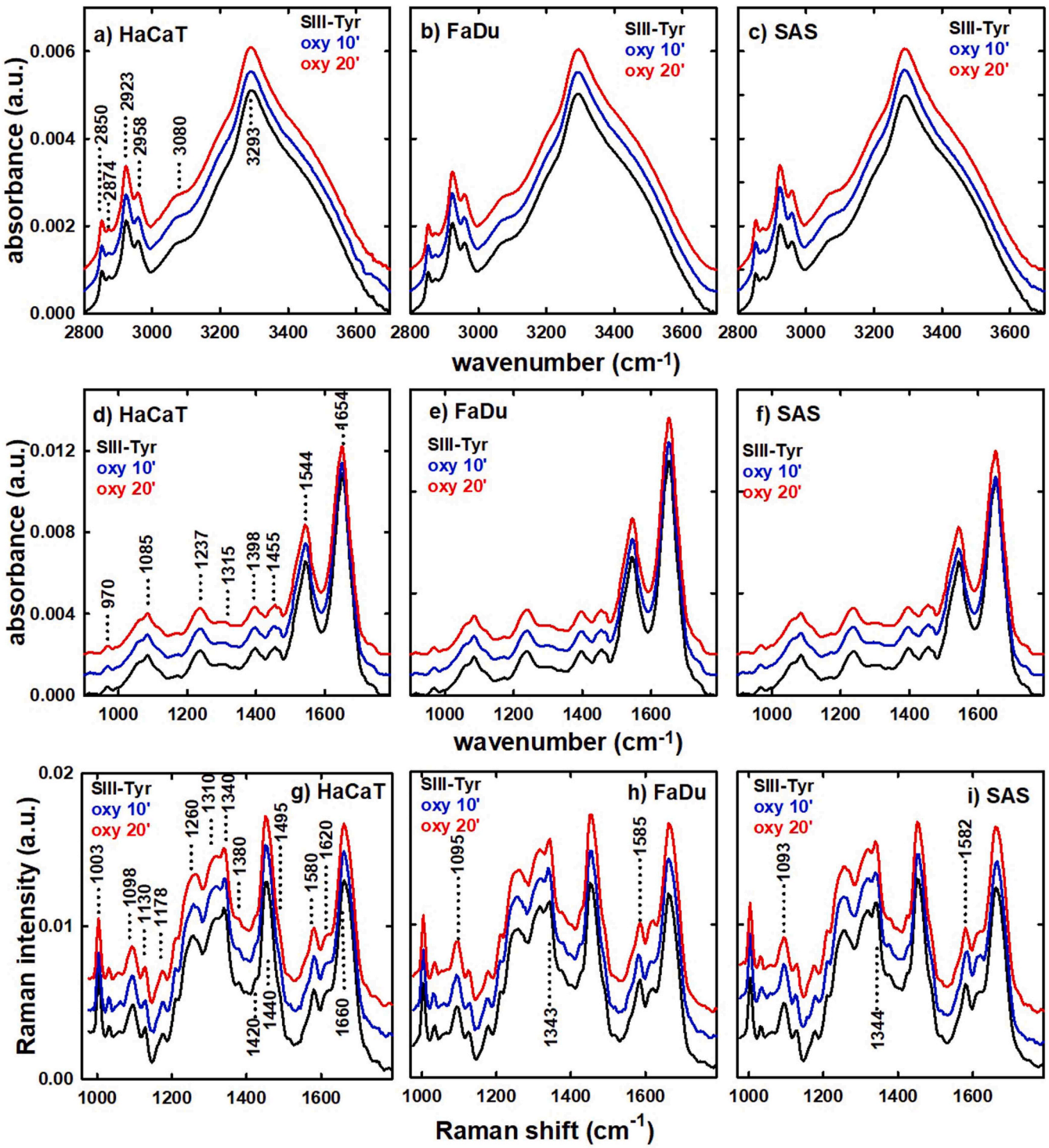

Fig. 3. Mean FTIR absorption spectra of HaCaT, FaDu and SAS cells incubated with SIII-Tyr solution and exposed to the PTWS oxy 10 min and 20 min in the 2800–3700 cm^{-1} range (a, b and c, respectively) and 900–1800 cm^{-1} range (d, e and f, respectively) and mean Raman spectra in the 980–1800 cm^{-1} range (g, h, i, respectively). The spectra have been intensity shifted for clarity. The labels in the HaCaT absorption and Raman spectra indicate the wavenumber position of the main spectral features.

Fig. 6a. The corresponding box plots clearly reveal a statistically significant difference in PC1 score values between cells exposed to air 20' sample and those incubated with SIII-Tyr or exposed to air 10' PTWS. By contrast, no statistically significant difference is observed between the PC1 score distributions of the SIII-Tyr group and the air 10' PTWS exposed cells. The loading 1 plot of Fig. 6b confirms that the decrease of methylene lipids bonds at 2850 and 2923 cm^{-1} following PTWS exposure is mainly responsible of such a discrimination, as occurs for oxy PTWS exposure. Similar observations can be made for FTIR spectra of HaCaT cells acquired in the 900–1800 cm^{-1} region (Fig. 6c and Fig. 6d). In this case, as well, a clear distinction is observed between the PC1 score values of cells exposed to air 20' PTWS and those of the other groups. Additionally, although the PC1 score distributions for SIII-Tyr and air 10' PTWS exposed cells are close together, they still differ by a

Table 2
Attribution of FTIR and Raman signals to the cellular components [43,44]. The main investigated spectral signals are highlighted with bold characters. Abbreviations: stretching (str.); symmetric (symm.); asymmetric (asymm.); twisting (twist.); wagging (wagg.).

FTIR position (cm^{-1})	Attribution lipids	Attribution proteins	Attribution nucleic acids
970			C-O, C-C str.
1085			PO_2 symm. str.
1237		C-OH str.	PO2 ¡ asymm. str.
1315		amide III	
1398	COO^- str.	COO^- str.	
1455	CH_3 bending	CH_3 bending	
1544		NH + XN βενδινγ αμιδε II	
1654		C═O amide I	
2850	CH_2 symm. str.		
2874	CH_3 symm. str.	CH_3 symm. str.	
2923	CH_2 asymm. str.		
2958	CH_3 asymm. str.	CH_3, asymm. str.	
3080		amide B	
3293		amide A	
Raman position (cm^{-1})	**Attribution lipids**	**Attribution proteins**	**Attribution nucleic acids**
1003		C-C str.	
1093÷1098		C-N str.	PO^-_2 str.
1130	C-C str.	C-N str.	
1178		C-H bending	
1260		amide III	
1310	CH_2 twist.		
1340÷1344		CH_2, CH_3 wagg.	CH_2, CH_3 wagg.
1380			ring breath. DNA
1420			ring breath. DNA
1440	CH_2 bending	CH_2 bending	
1495			ring breath. DNA
1580÷1585			ring breath. DNA
1620		C═C bending	
1660		Amide I	

small but statistically significant margin. Notably, the spectral features associated with nucleic acid components at 970 and 1085 cm^{-1} appear to play a minimal role in the discrimination between cells incubated with SIII-Tyr and those exposed to air 20' PTWS.

Similarly, the Raman spectra of the HaCaT cells exposed to PTWS air 20' are clearly distinguishable from those of the other experimental groups based on their PC3 score values, as shown in Fig. 6e. The loading 3 plot in Fig. 6f points out a decrease of the intensity of Raman signals due to the selected vibrational modes associated with nucleic acids components following exposure to PTWS air 20'. This behavior differs markedly from that observed with PTWS oxy treatment, where only the 1580 cm^{-1} signal showed a detectable change. These findings suggest that prolonged exposure to PTWS air may induce structural modifications to specific chemical bonds within nucleic acids in HaCaT cells. The most significant loading signals in Fig. 6f correspond to lipid (at about 1440 cm^{-1}) and protein (in the amide I and amide III regions): this confirms that these components are most affected by the exposure process. An important observation emerging from the comparison of PCA score plots in Figs. 5 and 6 is that significant biochemical alterations in HaCaT cells were observed only after 20 min of exposure to PTWS air. Indeed, both PC1 (as for FTIR spectra) and PC3 (as for Raman spectra) score values for HaCaT cells treated with PTWS air 10' are comparable to those of the control group (SIII-Tyr). This contrasts with the PTWS oxy conditions, where even shorter exposure times (10 min) led to detectable changes, as previously discussed.

The PCA score and loading plots of the FTIR spectra acquired on SIII-Tyr incubated FaDu cells and on those exposed to PTWS are displayed in Figs. 7 and 8. The score plot in Fig. 7a demonstrates that spectral differences between SIII-Tyr incubated cells and PTWS oxy ones within 2800–3700 cm^{-1} range occurs along the PC1 score values, similar to what was observed for HaCaT cells in Fig. 5a. Notably, the overlap between positive and negative values of PC1 score of PTWS oxy 10' and 20' is minimal and the difference in score distributions is not statistically significant. The loading 1 plot in Fig. 7b indicates that the peaks at 2850 and 2923 cm^{-1}, corresponding to CH_2 stretching of methylene lipids bonds, are involved in the spectra differences. Specifically, the relative intensity of these peaks is higher in PTWS-exposed cells compared to the SIII-Tyr controls, consistent with the trend observed for HaCaT cells.

In the 900–1800 cm^{-1} range (Fig. 7c), the PCA score plot highlights a clear and statistically significant separation between the FTIR spectra of SIII-Tyr and PTWS exposed FaDu cells according to the PC2 score values, while there is no statistically significant difference between the two distributions related to cells exposed to PTWS, as reported in Table 3. The loading 2 plot in Fig. 7d points out that the decrease of amide I and amide II bands due to exposure mainly cause the above separation, whereas small differences in the contributions from nucleic acid-related peaks are evident in Fig. 7d. The PC2 scores of PTWS exposed cells include both positive and negative values showing a partial overlap and thus precluding a definitive conclusion regarding the directionality of the changes in functional group content. Nonetheless, the score plot in Fig. 7c clearly shows that SIII-Tyr incubated and PTWS exposed cells are discriminated based on their FTIR spectra.

The score plot of Raman spectra acquired on FaDu cells exposed to PTWS oxy 10' and 20' is shown in Fig. 7e. As observed for HaCaT cells, the differentiation between the spectra of SIII-Tyr and PTWS exposed cells occurs according to the PC3 score values. Indeed, the PC3 score values of the spectra measured from the spectra of each of the three types of cells cluster separately but many overlaps occur between the distributions of PC3 score values related to the two types of PTWS exposed cells. The box plot in Fig. 7e and data reported in Table 3 highlight statistically significant differences between the distributions of PC3 score values of SIII-Tyr and PTWS oxy exposed cells, while the differences between the distributions of cells exposed to the two different PTWS oxy are not statistically significant. Such a behaviour suggests that biochemical modifications are induced by the action of PTWS oxy. In particular, the negative peaks at 1495 and 1585 cm^{-1} in the loading 3 plot in Fig. 7f indicate a modification of two among the four selected nucleic acid bonds following PTWS oxy exposure. The comparison between the loading 3 plot and the median values of the PC3 scores distribution (negative for scores of untreated SIII-Tyr incubated cells and positive for scores of PTWS exposed cells) implies a decrease of the intensity of the Raman signals related to some nucleic acid bonds as a consequence of exposure. Furthermore, the intense peaks at 1440 cm^{-1} and in the spectral range corresponding to the amide I vibrational mode in Fig. 7f confirm that the differences of PC3 score values shown in Fig. 7e can be mainly attributed to the reduction in the relative amount of CH bending and changes in protein bonds, respectively, as a consequence of PTWS exposure.

The results of PTWS air exposure of FaDu cells are reported in Fig. 8, which highlights the clustering and separation of the spectra related to SIII-Tyr incubated and PTWS exposed cells. In fact, the FTIR spectra of SIII-Tyr incubated cells in the 2800–3700 cm^{-1} range are characterized by negative values of PC1 score in Fig. 8a, while the spectra of cells exposed to PTWS air 20' have positive PC1 score values and the spectra of cells exposed to PTWS air 10' have both positive and negative values. The three score values distributions are well separated among them and the differences among the score values of the three distributions are statistically significant, as can be deduced in Table 3. The methylene lipids bonds at 2850 and 2923 cm^{-1} are the main responsible of the spectral differences (see loading 1 plot in Fig. 8b). In particular, the loading 1 plot and the signs of the median values of the PC1 score distributions indicate that the relative intensity of these peaks is larger in exposed cells than in control ones.

The score and loading plot in Figs. 8c and 8d, which are related to FTIR spectra of FaDu cells in the 900–1800 cm^{-1} range, are very similar to the corresponding plots in Figs. 7c and 7d obtained for PTWS oxy

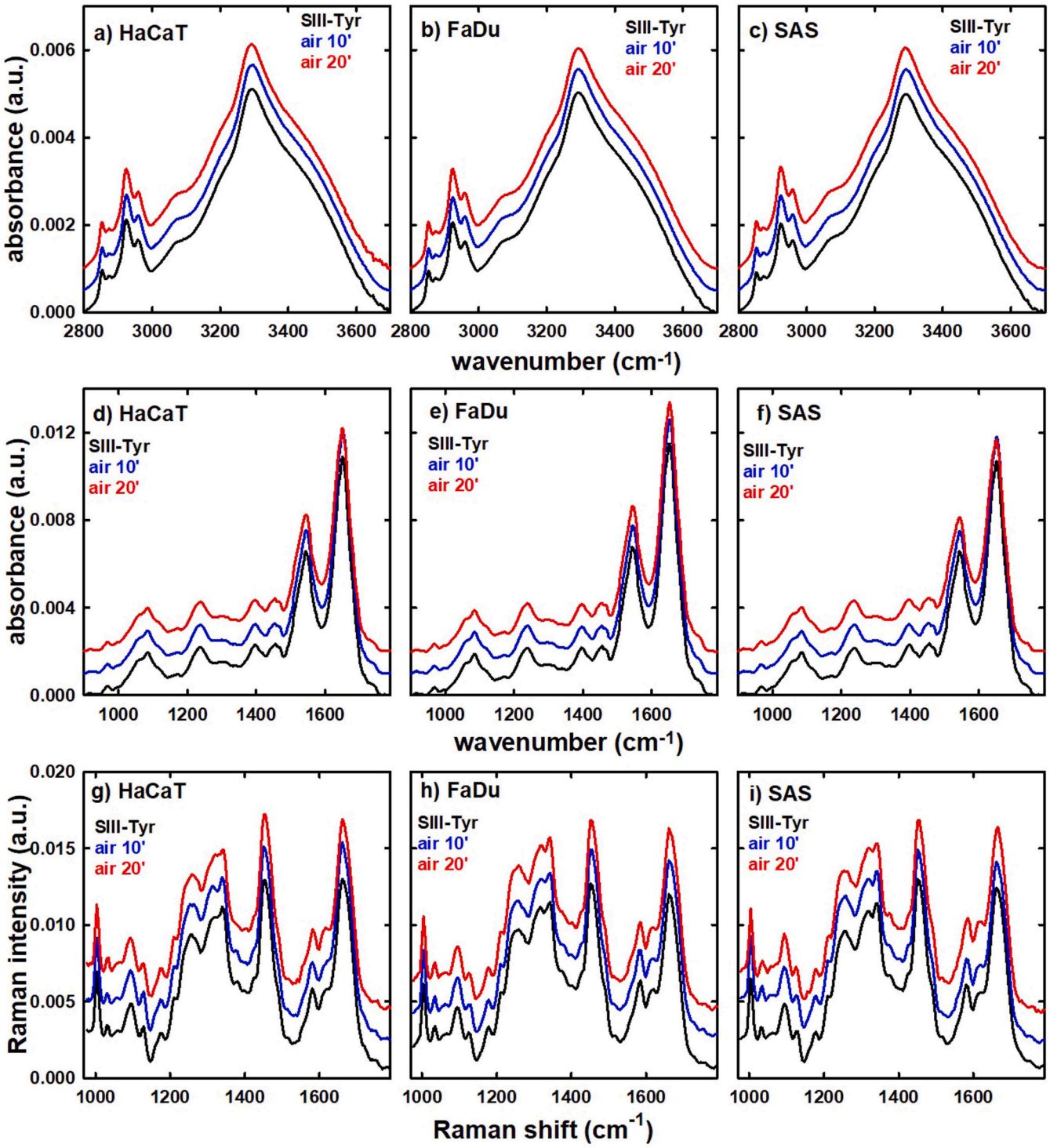

Fig. 4. Mean FTIR absorption spectra of HaCaT, FaDu and SAS cells incubated with SIII-Tyr solution and exposed to the PTWS air 10 min and 20 min in the 2800–3700 cm^{-1} range (a, b and c, respectively) and 900–1800 cm^{-1} range (d, e and f, respectively) and mean Raman spectra in the 980–1800 cm^{-1} range (g, h, i, respectively). The spectra have been intensity shifted for clarity.

exposure. Therefore, also for PTWS air exposure a clear discrimination between the spectra of SIII-Tyr incubated and PTWS exposed FaDu cells occurs and the contribution of the amide I and amide II absorption peaks to the spectral differences is evident (their intensities are lower in the spectra of cells PTWS exposed cells than in unexposed ones) whereas the FTIR signals related to nucleic acids appear to be unaffected by the exposure process.

The score and loading plot of Raman spectra from PTWS air exposed FaDu cells, shown in Figs. 8e and 8f, are characterized by an anomalous behaviour. In fact, the distribution of PC3 score values of SIII-Tyr incubated cells differs significantly from the corresponding distribution related to cells exposed to PTWS air 10', but it overlaps with that related to cells exposed to PTWS air 20'. However, the loading 3 plot in Fig. 8f suggest that the spectral signals related to nucleic acid components does not contribute significantly to the discrimination of the Raman spectra of untreated SIII-Tyr incubated cells from the Raman

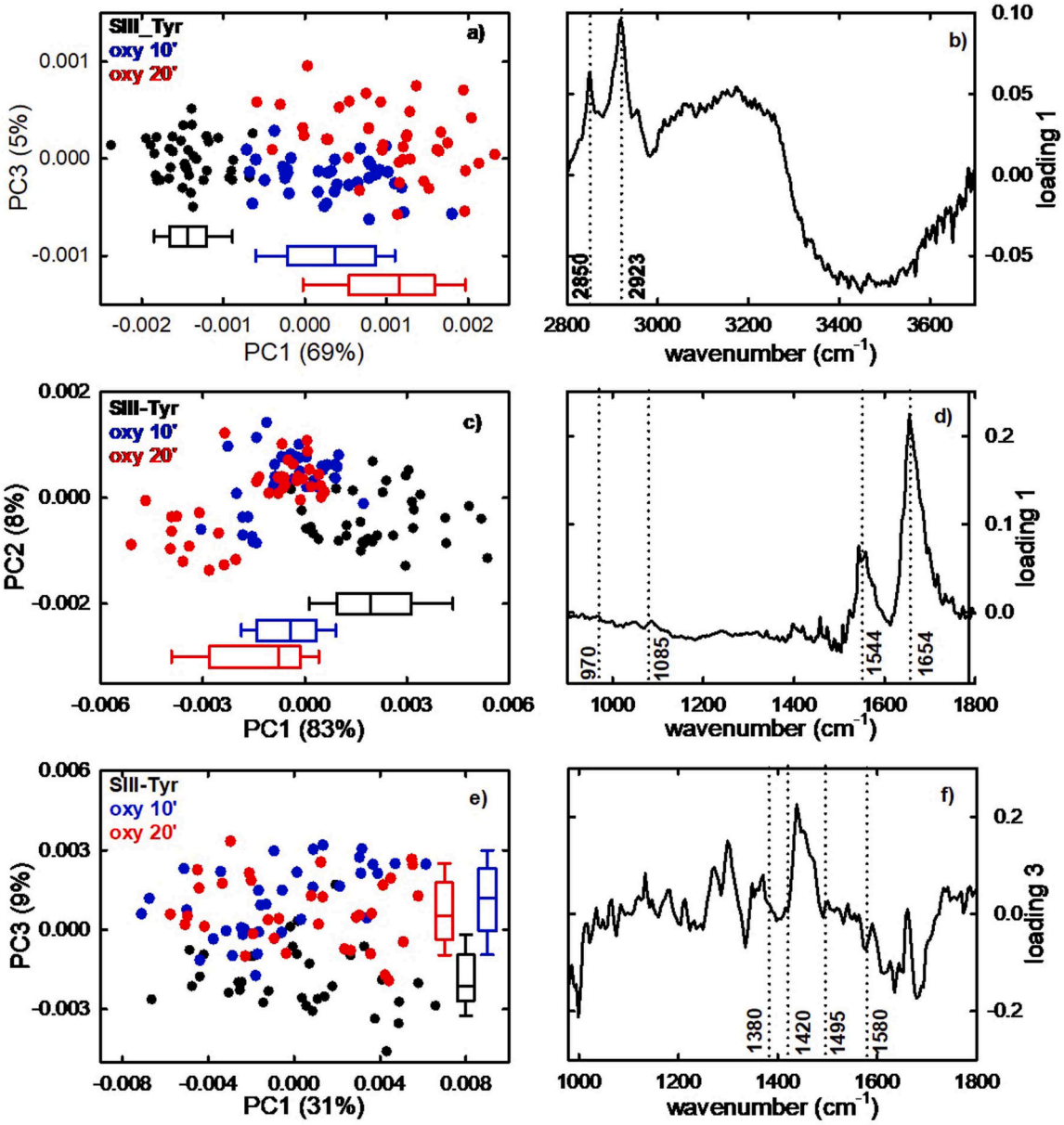

Fig. 5. PC score plots (left side) and loading spectra (right side) of the HaCaT cells incubated with SIII-Tyr solution and exposed to PTWS oxy 10 min and 20 min. The sections of the Figure are related to FTIR spectra measured in the 2800–3700 cm^{-1} range (a, b) and in the 900–1800 cm^{-1} range (c, d) and to Raman spectra (e, f). The line inside the box plots denotes the median value and the whiskers are drawn up to the largest data points that fall within 1.5 times the interquartile range. The dotted lines and labels in the loading plots correspond to wavenumber values bold marked in Table 2.

spectra of cells exposed to PTWS air 10' and air 20', respectively. Indeed, the loading 3 intensity values at the selected wavenumbers related to nucleic acid components are close to zero, except for the signal at 1585 cm^{-1}, which has a negative intensity value. Therefore, the nucleic acid components in FaDu cells probably are slightly affected by air-PTWS exposure. In contrast, the lipid and protein components are affected by PTWS exposure, as demonstrated by the loading 3 peaks at about 1440 and 1660 cm^{-1} .

The response of SAS cells to the PTWS oxy, reported in Figure S2, results similar to that of FaDu cells. In particular, the FTIR spectra in the 2800–3700 cm^{-1} range of SIII-Tyr incubated cells are well discriminated from those of both PTWS exposed cells based on the PC1 score values, whereas there is no statistically significant difference between the two distributions of PC1 score values related to the two types of PTWS exposed cells. The corresponding loading 1 plot shows that such a discrimination can be mainly ascribed to the lipid absorption peaks at 2850 and 2923 cm^{-1}, whose relative intensity increases following exposure to the two types of PTWS. Also, in the 900–1800 cm^{-1} range the score plot indicates that the spectra of SIII-Tyr incubated cells are quite discriminated from those of exposed ones. The differences among the three distributions of score values are statistically significant, although some overlapping between the PC1 score values of the spectra of SIII-Tyr incubated cells and those of a few spectra of the cells exposed to PTWS oxy 10 min occur. The loading 1 plot of the FTIR spectra in the in 900–1800 cm^{-1} range clearly evidences the prominent role of the amide I (at 1654 cm^{-1}) and amide II (at 1544 cm^{-1}) peaks in the discrimination between the spectra with mainly positive PC1 score value (related to SIII-Tyr incubated cells) and those with mainly negative score value (related to PTWS exposed cells): therefore, the relative intensity of such protein-related peaks decreases after PTWS exposure. In contrast, the contribution to discrimination resulting from the absorption of nucleic acid bonds is scarcely evident.

Table 3
Median, 25th and 75th percentile of the PC score distributions values of FTIR and Raman spectra measured for HaCaT, FaDu, and SAS cells exposed to different PTWS (oxy 10', oxy 20', air 10', and air 20') treatment. Cells exposed to untreated SIII-Tyr were used as control. The columns report the statistical difference between pairwise distributions, where * indicates a statistically significant difference with $p < 0.001$ and N indicates that the difference is not statistically significant.

HaCaT oxy												
cell exposure	*PC1·10^{-3} median (25th, 75th p.) FTIR 2800 3700 cm^{-1}*	*s*	*s*	*s*	*PC1·10^{-3} median (25th, 75th p.) FTIR 900–1800 cm^{-1}*	*s*	*s*	*s*	*PC3·10^{-3} median (25th, 75th p.) Raman 980–1800 cm^{-1}*	*s*	*s*	*s*
SIII-Tyr	**-1.44 (-1.66, −1.20)**	*	*		**1.92 (0.936, 3.12)**	*	*		**-2.13 (-2.68, −0.95)**	*	*	
oxy 10′	**0.36 (-0.22, 0.87)**	*		*	**-0.42 (-1.42, 0.34)**	*		**N**	**1.17 (-0.05, 2.30)**	*		**N**
oxy 20′	**1.16 (0.54, 1.59)**		*	*	**-0.78 (-2.82, −0.13)**		*	**N**	**0.52 (-0.368, 1.77)**		*	**N**
HaCaT air												
cell exposure	*PC1·10^{-3} median (25th, 75th p.) FTIR 2800 3700 cm^{-1}*	s	s	s	*PC1·10^{-3} median (25th, 75th p.) FTIR 900–1800 cm^{-1}*	s	s	s	*PC3·10^{-3} median (25th, 75th p.) Raman 980–1800 cm^{-1}*	s	s	s
SIII-Tyr	**-0.76 (-1.03, −0.55)**	**N**	*		**0.48 (-0.55, 1.66)**	*	*		**-1.26 (-2.42, 0.10)**	**N**	*	
air 10′	**-0.60 (-0.80, −0.42)**	**N**		*	**2.03 (1.08, 2.74)**	*		*	**-0.64, (-1.48, 0.07)**	**N**		*
air 20′	**1.33 (0.84, 1.85)**		*	*	**-2.98 (-3.68, −1.98**		*	*	**1.84 (0.25, 2.84)**		*	*
FaDu oxy												
cell exposure	*PC1·10^{-3} median (25th, 75th p.) FTIR 2800 3700 cm^{-1}*	s	s	s	*PC2·10^{-3} median (25th, 75th p.) FTIR 900–1800 cm^{-1}*	s	s	s	*PC3·10^{-3} median (25th, 75th p.) Raman 980–1800 cm^{-1}*	s	s	s
SIII-Tyr	**-0.70 (-0.96, −0.51)**	*	*		**0.69 (0.50, 0.95)**	*	*		**-1.51, (-2.75, −0.62)**	*	*	
oxy 10′	**0.21 (0.08, 0.46)**	*		**N**	**-0.18 (-0.40, 0.03)**	*		**N**	**0.38 (-0.56, 1.18)**	*		**N**
oxy 20′	**0.45 (0.32, 0.52)**		*	**N**	**-0.31 (-0.93, −0.06)**		*	**N**	**1.20 (-0.29, 2.51)**		*	**N**
FaDu air												
cell exposure	*PC1·10^{-3} median (25th, 75th p.) FTIR 2800 3700 cm^{-1}*	s	s	s	*PC2·10^{-3} median (25th, 75th p.) FTIR 900–1800 cm^{-1}*	s	s	s	*PC3·10^{-3} median (25th, 75th p.) Raman 980–1800 cm^{-1}*	s	s	s
SIII-Tyr	**-0.67 (-0.91, −0.49)**	*	*		**0.59 (0.34, 0.82)**	*	*		**-0.74 (-1.72, 0.30)**	*	**N**	
air 10′	**0.03 (-0.14, 0.12)**	*		*	**-0.01 (-0.42, 0.13)**	*		*	**1.31 (0.42, 2.05)**	*		**N**
air 20′	**0.58 (0.51, 0.80)**		*	*	**-0.37 (-0.59, −0.18)**		*	*	**-0.64 (-1.64, 1.62)**		**N**	**N**
SAS oxy												
cell exposure	*PC1·10^{-3} median (25th, 75th p.) FTIR 2800 3700 cm^{-1}*	s	s	s	*PC1·10^{-3} median (25th, 75th p.) FTIR 900–1800 cm^{-1}*	s	s	s	*PC4·10^{-3} median (25th, 75th p.) Raman 980–1800 cm^{-1}*	s	s	s
SIII-Tyr	**-1.62 (-1.82, −1.34)**	*	*		**3.24 (2.62. 3.86)**	*	*		**-1.79 (-2.41, −0.94)**	*	*	
oxy 10′	**0.98, (0.60, 1.41)**	*		**N**	**-2.29 (-4.61, −0.69)**	*		*	**1.12 (-0.15, 2.73)**	*		**N**
oxy 20′	**0.74 (0.46, 0.98)**		*	**N**	**-0.43 (-1.06, −0.07)**		*	*	**0.45 (-0.45, 1.37)**		*	**N**
SAS air												
cell exposure	*PC1·10^{-3} median (25th, 75th p.) FTIR 2800 3700 cm^{-1}*	s	s	s	*PC1·10^{-3} median (25th, 75th p.) FTIR 900–1800 cm^{-1}*	s	s	s	*PC3·10^{-3} median (25th, 75th p.) Raman 980–1800 cm^{-1}*	s	s	s
SIII-Tyr	**-0.99 (-1.27, −0.69)**	*	*		**1.59 (0.95, 2.26)**	**N**	*		**1.14 (-0.11, 2.83)**	*	*	
oxy 10′	**-0.32 (-0.58, −0.19)**	*		*	**1.87 (1.23, 3.34)**	**N**		*	**-0.16 (-0.70, 0.69)**	*		*
oxy 20′	**1.58 (1.08, 1.82)**		*	*	**-3.55 (-4.57, −2.80)**		*	*	**-1.40 (-2.56, −0.57)**		*	*

In addition, the PC4 score values differentiate the Raman spectra of SIII-Tyr incubated cells from those of PTWS oxy exposed ones. As reported above for the Raman spectra of HaCaT and FaDu cells, also in the case of SAS cells the positive and negative score values of the three types of cells partly overlap. Nonetheless, the three distributions of PC4 score values are characterized by negative and positive median values as far as the SIII-Tyr incubated and the PTWS exposed cells, respectively, is concerned. The corresponding loading 4 plot remarks that the relative intensity of the selected spectral signals related to nucleic acid components does not vary significantly in PTWS exposed cells compared to untreated SIII-Tyr incubated ones, except for the signal at 1380 cm^{-1}, whose intensity decreases following exposure. Instead, the largest differences between PTWS exposed and unexposed cells are found in the spectral region corresponding to protein components (at about 1620 and 1670 cm^{-1}).

Instead, the spectra of SAS cells after PTWS air exposure, reported in Figure S3, exhibit different characteristics than those of the corresponding HaCaT and FaDu cells. Indeed, the PC1 score values differentiates the FTIR spectra of cells exposed to PTWS air 20' from those of untreated SIII-Tyr incubated and PTWS air 10' exposed cells in the 2800–3700 cm^{-1} range. This behaviour is similar to that observed for HaCaT cells (see Fig. 6a). However, it is evident the significant statistical difference between the PC1 score distribution values of SIII-Tyr incubated and PTWS air 10' exposed SAS cells (see Table 3), although the median values of the two distributions are both negative. Instead, such significant statistical difference does not occur for the FTIR spectra of HaCaT cells. The corresponding loading 1 plot indicates that the peaks related to the methylene bonds of the lipid components are mainly responsible of the differentiation, being their intensity higher in SAS cells exposed to PTWS air 20' than in the other ones.

On the contrary, the FTIR spectra in the 900–1800 cm^{-1} range do not show statistically significant differences between the PC1 score values of SIII-Tyr incubated and PTWS air 10' exposed SAS cells, as also reported in Table 3. But both such distributions of PC1 score values are well differentiated from the distribution of PC1 score values of SAS cells exposed to PTWS air 20'. Thus, in 900–1800 cm^{-1} range the effect of SAS cell exposure is quite similar to that found for HaCaT cells and the protein related absorption peaks play the main role in the differentiation.

The score plot of Raman measurements of SAS cells exposed to air-PTWS in Figure S3 indicates that the PC3 score values mainly contribute to discriminate the SAS cells undergoing the three different treatments. The three distributions of PC3 score values partly overlap each other. Nonetheless, it is worth to remark that there is a statistically significant difference between the PC3 score value distributions of the SIII-Tyr incubated and PTWS air 10' exposed cells. Such a difference is not present for HaCaT cells in Fig. 6e. Considering the signs of the median values of the distributions, the loading 3 plot of Raman spectra shows that, among the selected Raman signals of characteristic nucleic acid bonds, only the signal at 1582 cm^{-1} is quite different from zero and,

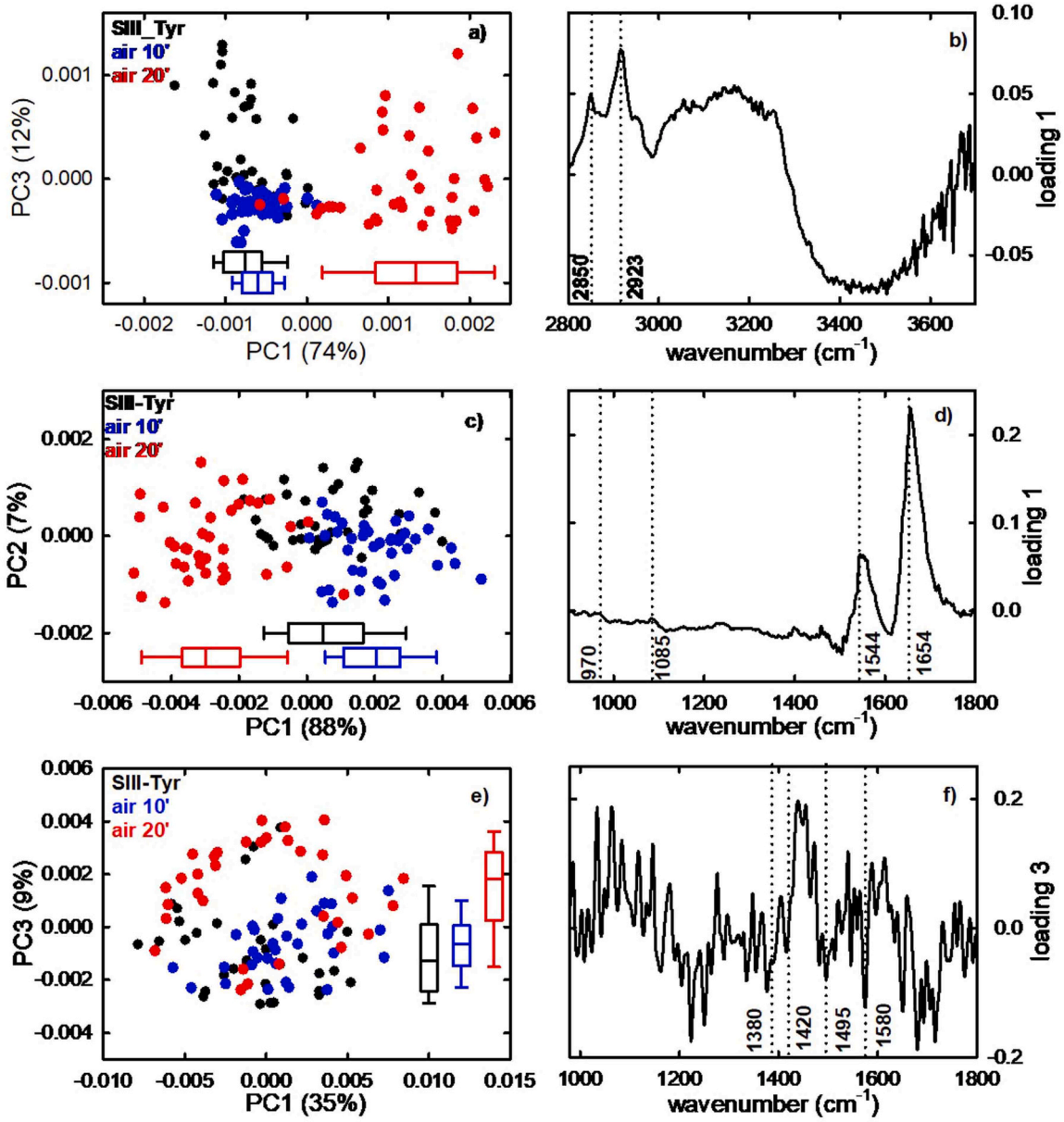

Fig. 6. PC score plots (left side) and loading spectra (right side) of the HaCaT cells incubated with the SIII-Tyr solution and exposed to PTWS air 10' and 20'. The sections of the Figure are related to FTIR spectra measured in the 2800–3700 cm^{-1} range (a, b) and in the 900–1800 cm^{-1} range (c, d) and to Raman spectra (e, f). The line inside the box plots denotes the median value and the whiskers are drawn up to the largest data points that fall within 1.5 times the interquartile range. The dotted lines and labels in the loading plots correspond to wavenumber values bold marked in Table 2.

consequently, it suggests a modification of such a bond after the action of the PTWS air 20'. In agreement with the findings of the FTIR spectral analysis, the loading signals corresponding to lipid (at 1440 cm^{-1}) and protein (at 1004 cm^{-1} and in the amide I range) peaks are characterized by large intensity; therefore, these components play the main role in distinguishing between PTWS exposed and unexposed cells.

Overall, it can be stated that vibrational spectroscopy analysis (FTIR and Raman) revealed that exposure to different PTWS formulations induces measurable biochemical alterations in both healthy (HaCaT) and cancerous (FaDu, SAS) cell lines. These changes are dependent on treatment duration and gas composition (oxy vs. air), with more pronounced effects observed following 20-minute treatments. The most significant alterations involved lipid membrane components, particularly CH_2 stretching vibrations, indicating oxidative stress and lipid peroxidation. FTIR spectra showed clear discrimination between treated and untreated cells, both in the 2800–3700 cm^{-1} and 900–1800 cm^{-1} regions, mainly due to variations in lipid and protein-related signals, respectively. No modification was evident in the C-O, C-C and phosphate bonds of nucleic acid components. Raman spectroscopy, despite a lower signal-to-noise ratio, revealed nucleic acid alterations, especially in HaCaT and to a lesser extend in SAS cells after PTWS 20 min exposure. Overall, the data confirm that PTWS induces cell type– and condition–specific oxidative responses, which can be effectively monitored via vibrational spectroscopy.

4. Conclusions

In conclusion, this study establishes FTIR and Raman spectroscopy as primary, label-free readouts to map PTWS-induced biochemical remodelling in healthy versus HNC cells. The multi-diagnostic approach proposed provides a robust and multidimensional framework for interpreting cellular responses to oxidative stress. The combination of the

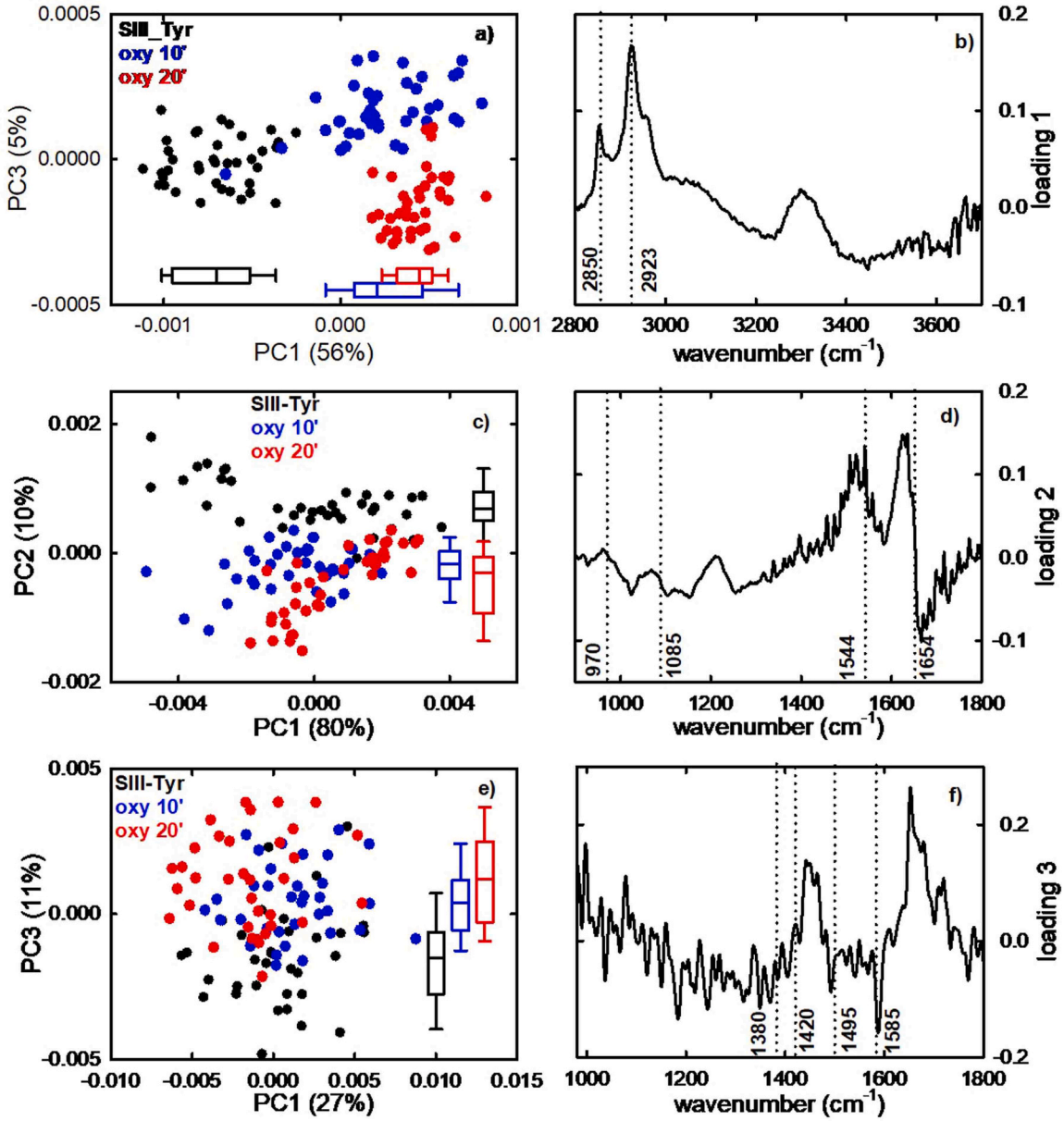

Fig. 7. PC score plots (left side) and loading spectra (right side) of the FaDu cells incubated with the SIII-Tyr solution and exposed to PTWS oxy 10 min and 20 min. The sections of the Figure are related to FTIR spectra measured in the 2800–3700 cm^{-1} range (a, b) and in the 900–1800 cm^{-1} range (c, d) and to Raman spectra (e, f). The line inside the box plots denotes the median value and the whiskers are drawn up to the largest data points that fall within 1.5 times the interquartile range. The dotted lines and labels in the loading plots correspond to wavenumber values bold marked in Table 2.

techniques demonstrated that molecular fingerprints coherently reflect functional outcomes, revealing a limited impact of PTWS on HaCaT, alongside a marked susceptibility of FaDu and SAS cell lines. This differential response is further supported by condition-dependent increases in intracellular ROS levels: HNC cell lines displayed more pronounced spectral alterations than HaCaT, with the largest effects after PTWS oxy 20' treatment and a still-discernible window of selectivity after exposure to air 10' formulations. A key advancement of this work lies in the integration of PCA analysis applied to both FTIR and Raman datasets, enabling a systematic and quantitative dissection of biochemical changes. From a biochemical perspective, PTWS exposure induced a consistent remodeling of lipid and protein components, with an increase in lipid-related signals and a concomitant decrease in protein-associated bands. In contrast, nucleic acids appear only moderately affected, as not all representative vibrational modes exhibit significant variation, except in specific conditions such as HaCaT cells exposed to air 20' PTWS. These findings support a mechanistic link between spectroscopic shifts and selective cytotoxicity. The integration of FTIR and Raman spectroscopy proves particularly advantageous: FTIR offers high signal-to-noise ratio over large sample areas with strong sensitivity to lipids and proteins, whereas Raman provides subcellular spatial resolution and enhanced selectivity toward nucleic acid variations. Together these techniques establish practical endpoints to monitor cellular responses and guide the rational optimization of PTWS generation parameters (i.e. gas feed and treatment time) for selective anticancer activity. Collectively, PCA highlights a coordinated modulation of lipids, proteins, and nucleic acids. As PTWS function as exogenous sources of RONS and thereby drive cellular oxidative stress, the combined application of FTIR and Raman spectroscopy may, in the next future, offer a powerful diagnostic strategy for therapeutic approaches based on redox medicine, including those employed in oncology. Validation could proceed by extending the spectral panel, including longitudinal/live-cell

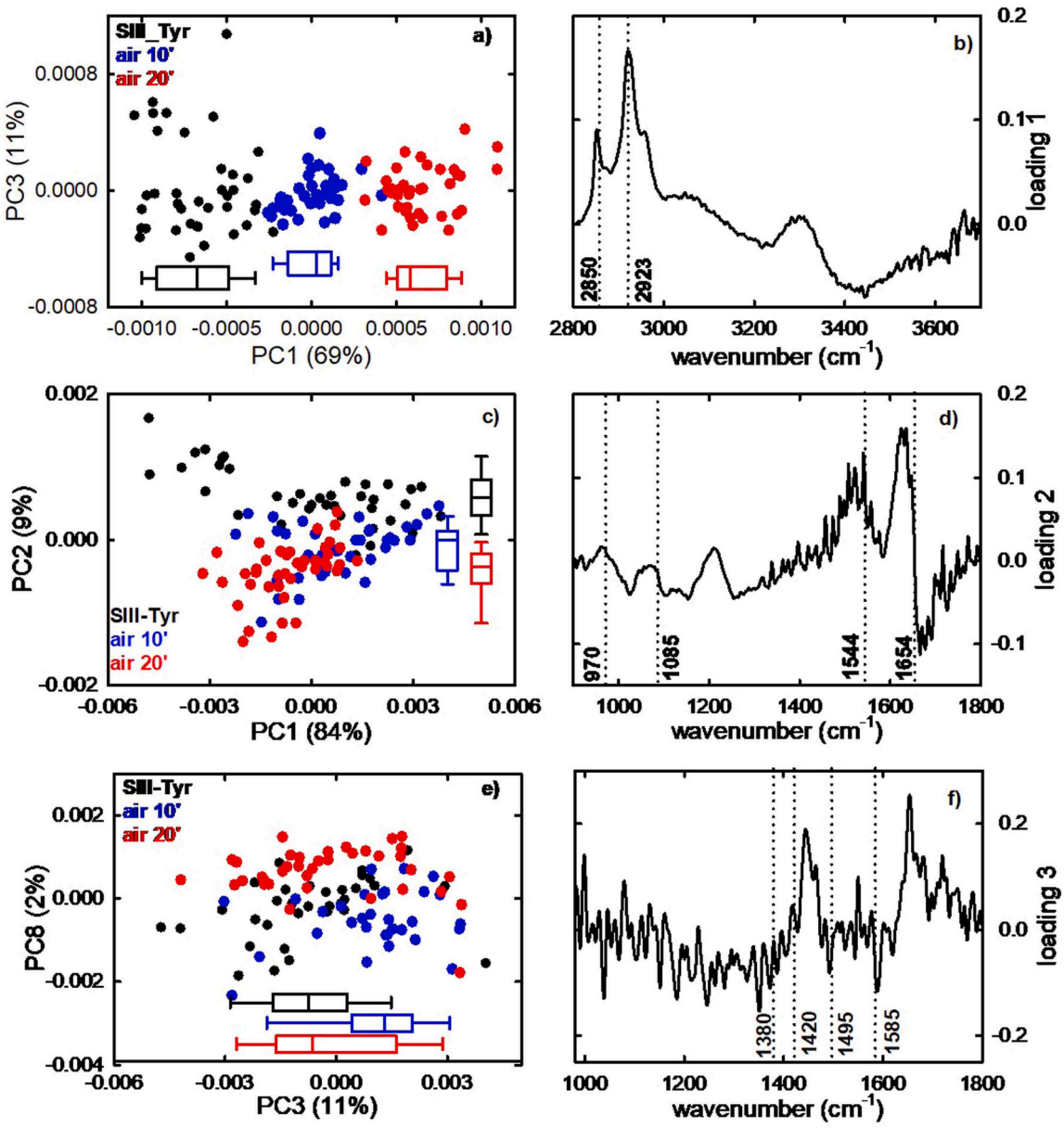

Fig. 8. PC score plots (left side) and loading spectra (right side) of the FaDu cells incubated with the SIII-Tyr solution and exposed to PTWS air 10' and 20'. The sections of the Figure are related to FTIR spectra measured in the 2800–3700 cm^{-1} range (a, b) and in the 900–1800 cm^{-1} range (c, d) and to Raman spectra (e, f). The line inside the box plots denotes the median value and the whiskers are drawn up to the largest data points that fall within 1.5 times the interquartile range. The dotted lines and labels in the loading plots correspond to wavenumber values bold marked in Table 2.

acquisitions, and testing additional HNC subtypes to consolidate translation toward preclinical validation. While this study was conducted on in vitro cell line models, which provide a controlled environment for mechanistic insights, future work could extend these observations to more complex in vivo systems. Only selected long-lived reactive species (H_2O_2 and NO_2^-) were quantified in the present study, providing a focused view of oxidative effects; further investigations could expand the panel of monitored species to deepen mechanistic understanding. Importantly, PCA offered a robust exploratory tool to highlight key spectral changes and sample differentiation, laying the groundwork for more detailed analyses in future studies.

CRediT authorship contribution statement

Vittoria Perrotti: Writing – review & editing, Supervision, Funding acquisition, Conceptualization. **Giuseppe Perna:** Writing – review & editing, Validation, Supervision, Investigation, Formal analysis. **Roberto Gristina:** Writing – review & editing, Investigation. **Savino Cosmai:** Investigation. **Maria Lasalvia:** Writing – original draft, Investigation, Data curation. **Vito Carlo Alberto Caponio:** Writing – review & editing, Data curation. **Anna Martina Battaglia:** Writing – original draft, Investigation, Formal analysis, Data curation. **Eloisa Sardella:** Writing – review & editing, Visualization, Validation, Supervision, Conceptualization. **Vito Capozzi:** Supervision. **Flavia Biamonte:** Writing – original draft, Investigation, Formal analysis, Data curation.

Declaration of Competing Interest

The authors declare that they have no known competing financial interests or personal relationships that could have appeared to influence the work reported in this paper.

Acknowledgements

This research was funded by PRINPNRR 2022-P2022F4P8P-BifunctioNal plasma-treated solutions as a new thErapeutiC Tool for cAnceR (NECTAR). We thank COST Actions CA20114 (Therapeutical Applications of Cold Plasmas) for the stimulating environment provided.

Appendix A. Supporting information

Supplementary data associated with this article can be found in the online version at doi:10.1016/j.vibspec.2026.103913.

Data availability

Data will be made available on request.

References

[1] F. Bray, J. Ferlay, I. Soerjomataram, R.L. Siegel, L.A. Torre, A. Jemal, Global cancer statistics 2018: GLOBOCAN estimates of incidence and mortality worldwide for 36 cancers in 185 countries, CA A Cancer J. Clin. 68 (6) (2018) 394–424, https://doi.org/10.3322/caac.21492.

[2] V. Perrotti, V.C.A. Caponio, L.L. Muzio, E.H. Choi, M.C. Di Marcantonio, M. Mazzone, N.K. Kaushik, G. Mincione, Open questions in cold atmospheric plasma treatment in head and neck cancer: a systematic review, Int J. Mol. Sci. 23 (18) (2022) 10238, https://doi.org/10.3390/ijms231810238.

[3] https://www.nccn.org/guidelines/guidelines-detail?category=1&id=1437 accessed on June 24th 2025.

[4] J.P. Machiels, C. René Leemans, W. Golusinski, C. Grau, L. Licitra, V. Gregoire, E.H. N.S. Executive Board, E.S.M.O. Guidelines Committee, E.S.T.R.O. Executive Board, Reprint of "Squamous cell carcinoma of the oral cavity, larynx, oropharynx and hypopharynx: EHNS-ESMO-ESTRO Clinical Practice Guidelines for diagnosis, treatment and follow-up", Oral. Oncol. 113 (2021) 105042, https://doi.org/10.1016/j.oraloncology.2020.105042.

[5] A. Mordzińska-Rak, I. Telejko, G. Adamczuk, T. Trombik, A. Stepulak, E. Błaszczak, Advancing head and neck cancer therapies: from conventional treatments to emerging strategies, Biomedicines 13 (5) (2025) 1046, https://doi.org/10.3390/biomedicines13051046.

[6] G. Gatta, R. Capocaccia, L. Botta, S. Mallone, R. De Angelis, E. Ardanaz, H. Comber, N. Dimitrova, M.K. Leinonen, S. Siesling, J.M. van der Zwan, L. Van Eycken, O. Visser, M.P. Žakelj, L.A. Anderson, F. Bella, I. Kaire, R. Otter, C.A. Stiller, A. Trama, RARECAREnet working group. Burden and centralised treatment in Europe of rare tumours: results of RARECAREnet-a population-based study, Lancet Oncol. 18 (8) (2017) 1022–1039, https://doi.org/10.1016/S1470-2045(17)30445-X. Epub 2017 Jul 4. Erratum in: *Lancet Oncol.* 2017, 18(8): e433. doi: 10.1016/S1470-2045(17)30531-4.

[7] M.L. Semmler, S. Bekeschus, M. Schäfer, T. Bernhardt, T. Fischer, K. Witzke, C. Seebauer, H. Rebl, E. Grambow, B. Vollmar, et al., Molecular mechanisms of the efficacy of cold atmospheric pressure plasma (CAP) in cancer treatment, Cancers 12 (2020) 269, https://doi.org/10.3390/cancers12020269.

[8] P.G. Subramanian, A. Jain, A.M. Shivapuji, N.R. Sundaresan, S. Dasappa, L. Rao, Plasma-activated water from a dielectric barrier discharge plasma source for the selective treatment of cancer cells, Plasma Process. Polym. 17 (8) (2020) 1900260, https://doi.org/10.1002/ppap.201900260.

[9] V. Veronico, S. Morelli, A. Piscioneri, R. Gristina, M. Casiello, P. Favia, V. Armenise, F. Fracassi, L. De Bartolo, E. Sardella, Anticancer effects of plasma-treated water solutions from clinically approved infusion liquids supplemented with organic molecules, ACS Omega 8 (37) (2023) 33723–33736, https://doi.org/10.1021/acsomega.3c04061.

[10] N. Gelbrich, L. Miebach, J. Berner, E. Freund, F. Saadati, A. Schmidt, M. Stope, U. Zimmermann, M. Burchardt, S. Bekeschus, Medical gas plasma augments bladder cancer cell toxicity in preclinical models and patient-derived tumor tissues, J. Adv. Res 47 (2023) 209–223, https://doi.org/10.1016/j.jare.2022.07.012.

[11] Y. Li, Y. Lv, Y. Zhu, X. Yang, B. Lin, M. Li, Y. Zhou, Z. Tan, E.H. Choi, J. Wang, S. Wang, Y. Liu, Low-temperature plasma-activated medium inhibited proliferation and progression of lung cancer by targeting the PI3K/Akt and MAPK pathways, Oxid. Med Cell Longev. 18 (2022) 9014501, https://doi.org/10.1155/2022/9014501.

[12] J. Pan, Y.L. Li, C.M. Liu, Y. Tian, S. Yu, K.L. Wang, J. Zhang, J. Fang, Investigation of cold atmospheric plasma-activated water for the dental unit waterline system contamination and safety evaluation in vitro, Plasma Chem. Plasma Process 37 (2017) 1091–1103, https://doi.org/10.1007/s11090-017-9811-0.

[13] X. Su, Y. Tian, H. Zhou, Y. Li, Z. Zhang, B. Jiang, B. Yang, J. Zhang, J. Fang, Inactivation efficacy of nonthermal plasma-activated solutions against newcastle disease virus, Appl. Environ. Microbiol 84 (2018) e02836-17, https://doi.org/10.1128/AEM.02836-17.

[14] D. Xu, S. Wang, B. Li, M. Qi, R. Feng, Q. Li, H. Zhang, H. Chen, M.G. Kong, Effects of plasma-activated water on skin wound healing in mice, Microorganisms 8 (2020) 1091, https://doi.org/10.3390/microorganisms8071091.

[15] K. Sklias, J.S. Sousa, P.-M. Girard, Role of short- and long-lived reactive species on the selectivity and anti-cancer action of plasma treatment in vitro, Cancers 13 (2021) 615, https://doi.org/10.3390/cancers13040615.

[16] E. Sardella, V. Veronico, R. Gristina, L. Grossi, S. Cosmai, M. Striccoli, M. Buttiglione, F. Fracassi, P. Favia, Plasma treated water solutions in cancer treatments: the contrasting role of RNS, Antioxidants 10 (2021) 605, https://doi.org/10.3390/antiox10040605.

[17] L. Miebach, H. Mohamed, K. Wende, V. Miller, S. Bekeschus, Pancreatic cancer cells undergo immunogenic cell death upon exposure to gas plasma-oxidized ringers lactate, Cancers 15 (2023) 319, https://doi.org/10.3390/cancers15010319.

[18] J. Van Loenhout, T. Flieswasser, L. Freire Boullosa, J. deWaele, J. van Audenaerde, E. Marcq, J. Jacobs, A. Lin, E. Lion, H. Dewitte, et al., Cold atmospheric plasma-treated pbs eliminates immunosuppressive pancreatic stellate cells and induces immunogenic cell death of pancreatic cancer cells, Cancers 11 (2019) 1597, https://doi.org/10.3390/cancers11101597.

[19] D. Boehm, J. Curtin, P.J. Cullen, P. Bourke, Hydrogen peroxide and beyond-the potential of high-voltage plasma-activated liquids against cancerous cells, Anti-Cancer Agents Med. Chem. (Former. Curr. Med. Chem.-Anti-Cancer Agents) 18 (6) (2018) 815–823, https://doi.org/10.2174/1871520617666170801110517.

[20] T. von Woedtke, S. Bekeschus, K.-D. Weltmann, K. Wende, Plasma-treated liquids for medicine: a narrative review on state and perspectives, Plasma Process. Polym. 22 (2025) 2400255, https://doi.org/10.1002/ppap.202400255.

[21] A.M. Battaglia, A. Sacco, E. Vecchio, S. Scicchitano, L. Petriaggi, E. Giorgio, S. Bulotta, S. Levi, C.M. Faniello, F. Biamonte, F. Costanzo, Iron affects the sphere-forming ability of ovarian cancer cells in non-adherent culture conditions, Front Cell Dev. Biol. 11 (2023) 1272667, https://doi.org/10.3389/fcell.2023.1272667.

[22] J. Striesow, Z. Nasri, T. von Woedtke, S. Bekeschus, K. Wende, Epilipidomics reveals lipid fatty acid and headgroup modification in gas plasma-oxidized biomembranes, Redox Biol. 77 (2024) 103343, https://doi.org/10.1016/j.redox.2024.103343.

[23] Alessandra Altomare, Giovanna Baron, Erica Gianazza, Cristina Banfi, Marina Carini, Giancarlo Aldini, Lipid peroxidation derived reactive carbonyl species in free and conjugated forms as an index of lipid peroxidation: limits and perspectives, Redox Biol. 42 (2021) 101899, https://doi.org/10.1016/j.redox.2021.101899.

[24] P.V. Escribá, X. Busquets, J. Inokuchi, G. Balogh, Z. Török, I. Horváth, J. L. Harwood, L. Vígh, Membrane lipid therapy: modulation of the cell membrane composition and structure as a molecular base for drug discovery and new disease treatment, Prog. Lipid Res 59 (2015) 38–53, https://doi.org/10.1016/j.plipres.2015.04.003.

[25] D. Traynor, I. Behl, D. O'Dea, F. Bonnier, S. Nicholson, F. O'Connell, A. Maguire, S. Flint, S. Galvin, C.M. Healy, C.M. Martin, J.J. O'Leary, A. Malkin, H.J. Byrne, F. M. Lyng, Raman spectral cytopathology for cancer diagnostic applications, Nat. Protoc. 16 (7) (2021) 3716–3735, https://doi.org/10.1038/s41596-021-00559-5.

[26] M. Lasalvia, V. Capozzi, G. Perna, Classification of healthy and cancerous colon cells by Fourier transform infrared spectroscopy, Spectrochim. Acta A Mol. Biomol. Spectrosc. 321 (2024) 124683, https://doi.org/10.1016/j.saa.2024.124683.

[27] Natalia Galant, Marcin Nicoś, Maryna Khalavka, Natalia Krzyżanowska, Izabela Chmielewska, Barbara Kuźnar-Kamińska, Paweł. Krawczyk, Anna Sroka-Bartnicka, Joanna Depciuch, Biochem. Biophys. Res. Commun. 771 (2025) 152007, https://doi.org/10.1016/j.bbrc.2025.152007.

[28] Ao Song, Wanli Yang, Jun Wang, Yisa Cai, Lizheng Cai, Nan Pang, Ruihua Yu, Zhikun Liu, Chao Yang, Feng Jiang, SLAS Technol. 31 (2025) 100253, https://doi.org/10.1016/j.slast.2025.100253.

[29] Cai Li Song, Sergei G. Kazarian, Micro ATR-FTIR spectroscopic imaging of colon biopsies with a large area Ge crystal, Spectrochim. Acta Part A Mole. BioMole. Spectrosc. 228 (2020) 117695, https://doi.org/10.1016/j.saa.2019.117695.

[30] E. Kaznowska, J. Depciuch, K. Szmuc, J. Cebulski, Use of FTIR spectroscopy and PCA-LDC analysis to identify cancerous lesions within the human colon, J. Pharm. Biomed. Anal. 134 (2017) 259–268, https://doi.org/10.1016/j.jpba.2016.11.047.

[31] Beata Brozek-Pluska, Adam Dziki, Halina Abramczyk, Virtual spectral histopathology of colon cancer - biomedical applications of Raman spectroscopy and imaging, J. Mol. Liq. 303 (2020) 112676, https://doi.org/10.1016/j.molliq.2020.112676.

[32] T.H. Dakhakhni, D. Alsufyani, Biophysical investigation to assess the toxicity of the herbicide 2, 4-dichlorophenoxyacetic acid on rats blood serum: a FTIR spectroscopic study, SN Appl. Sci. 5 (2023) 270, https://doi.org/10.1007/s42452-023-05494-6.

[33] G. Perna, V. Capozzi, M. Lasalvia, Vitro Detection of Biochemical Effect in Human CaCo-2 Cell Line after Exposure to a Low Concentration of a Deltamethrin-Based Pesticide, Chemosensors 10 (2022) 438, https://doi.org/10.3390/chemosensors10110438.

[34] F. Faghihzadeh, N.M. Anaya, L.A. Schifman, et al., Fourier transform infrared spectroscopy to assess molecular-level changes in microorganisms exposed to nanoparticles, Nanotechnol. Environ. Eng. 1 (1) (2016), https://doi.org/10.1007/s41204-016-0001-8.

[35] R.R. Jones, D.C. Hooper, L. Zhang, D. Wolverson, V.K. Valev, Raman Techniques: Fundamentals and Frontiers, Nanoscale Res Lett. 14 (1) (2019) 231, https://doi.org/10.1186/s11671-019-3039-2.

[36] V. Veronico, P. Favia, F. Fracassi, R. Gristina, E. Sardella, Validation of colorimetric assays for hydrogen peroxide, nitrate and nitrite ions in complex plasma-treated water solutions, Plasma Process. Polym. 18 (2021) 2100062, https://doi.org/10.1002/ppap.202100062.

[37] R. Chirillo, I. Aversa, A. Di Vito, A. Salatino, A.M. Battaglia, A. Sacco, M.A. Di Sanzo, M.C. Faniello, B. Quaresima, C. Palmieri, F. Biamonte, F. Costanzo, FtH-

Mediated ROS Dysregulation Promotes CXCL12/CXCR4 Axis Activation and EMT-Like Trans-Differentiation in Erythroleukemia K562 Cells, Front Oncol. 10 (2020) 698, https://doi.org/10.3389/fonc.2020.00698.
[38] M. Di Sanzo, F. Cozzolino, A.M. Battaglia, I. Aversa, V. Monaco, A. Sacco, F. Biamonte, C. Palmieri, F. Procopio, G. Santamaria, F. Ortuso, P. Pucci, M. Monti, M.C. Faniello, Ferritin heavy chain binds peroxiredoxin 6 and inhibits cell proliferation and migration, Int J. Mol. Sci. 23 (21) (2022) 12987, https://doi.org/10.3390/ijms232112987.
[39] Menges, F. Spectragryph—Optical Spectroscopy Software, Version 1.2.16; Spectragryph: Oberstdorf, Germany, 2023. Available online: ⟨http://www.effemm2.de/spectragryph/⟩(accessed on 10 February 2025).
[40] G. Perna, M. Lasalvia, V. Capozzi, Raman microspectroscopy discrimination of single human keratinocytes exposed at low dose of pesticide, J. Mol. Struct. 1010 (2012) 123–129, https://doi.org/10.1016/j.molstruc.2011.11.042.
[41] J. Demsar, T. Curk, A. Erjavec, C. Gorup, T. Hocevar, M. Milutinovic, M. Mozina, M. Polajnar, M. Toplak, A. Staric, M. Stajdohar, L. Umek, L. Zagar, J. Zbontar, M. Zitnik, B. Zupan, Orange: Data Mining Toolbox in Python, J. Mach. Learn. Res. 14 (2013) 2349–2353.
[42] F. Tampieri, Y. Gorbanev, E. Sardella, Plasma-treated liquids in medicine: let's get chemical, Plasma Process. Polym. 20 (2023) e2300077, https://doi.org/10.1002/ppap.202300077.
[43] A.C.S. Talari, M.A.G. Martinez, Z. Movasaghi, S. Rehman, I.U. Rehman, Advances in Fourier transform infrared (FTIR) spectroscopy of biological tissues, Appl. Spectrosc. Rev. 52 (5) (2017) 456–506, https://doi.org/10.1080/05704928.2016.1230863.
[44] A.C.S. Talari, Z. Movasaghi, S. Rehman, I. ur Rehman, Raman spectroscopy of biological tissues, Appl. Spectrosc. Rev. 50 (2015) 46–111, https://doi.org/10.1080/05704928.2014.923902.
[45] E.A. Taylor, E. Donnelly, Raman and Fourier transform infrared imaging for characterization of bone material properties, Bone 139 (2020) 115490, https://doi.org/10.1016/j.bone.2020.115490.
[46] F.S. Ruggeri, C. Marcott, S. Dinarelli, G. Longo, M. Girasole, G. Dietler, T.P. J. Knowles, Identification of oxidative stress in red blood cells with nanoscale chemical resolution by infrared nanospectroscopy, Int J. Mol. Sci. 19 (9) (2018) 2582, https://doi.org/10.3390/ijms19092582.
[47] B. Vileno, S. Jeney, A. Sienkiewicz, P.R. Marcoux, L.M. Miller, L. Forró, Evidence of lipid peroxidation and protein phosphorylation in cells upon oxidative stress photo-generated by fullerols, Biophys. Chem. 152 (1–3) (2010) 164–169, https://doi.org/10.1016/j.bpc.2010.09.004.
[48] Madhuree Kumari, Siya Kamat, C. Jayabaskaran, Usnic acid induced changes in biomolecules and their association with apoptosis in squamous carcinoma (A-431) cells: A flow cytometry, FTIR and DLS spectroscopic study, Spectrochim. Acta Part A Mol. Biomol. Spectrosc. 274 (2022) 121098, https://doi.org/10.1016/j.saa.2022.121098.
[49] Silvia Gaudenzi, Deleana Pozzi, Paolo Toro, Ida Silvestri, Stefania Morrone, Agostina Congiu Castellano, Cell apoptosis specific marker found by Fourier Transform Infrared Spectroscopy, J. Spectrosc. 18 (2004) 483591, https://doi.org/10.1155/2004/483591.
[50] S. Saladrigas-Manjón, T. Dučić, L. Galindo, C. Fernández-Avilés, V. Pérez, R. de la Torre, P. Robledo, Effects of Cannabis Use on the Protein and Lipid Profile of Olfactory Neuroepithelium Cells from Schizophrenia Patients Studied by Synchrotron-Based FTIR Spectroscopy, Biomolecules 10 (2) (2020) 329, https://doi.org/10.3390/biom10020329.
[51] V. di Giacomo, M. Balaha, A. Pece, I. Cela, G. Fulgenzi, G. Orsini, T. Spadoni, T. R. Acharya, N.K. Kaushik, E.H. Choi, M. Rapino, M. Mazzone, G. Mincione, G. Sala, E. Sardella, V. Perrotti, Human head and neck cancer cell lines response to cold atmospheric plasma activated media is affected by the chemistry of culture media, Heliyon 11 (1) (2024) e41458, https://doi.org/10.1016/j.heliyon.2024.e41458.